Supporting Information

Unlocking Structural Diversity in Gold(III) Hydrides: Unexpected Interplay of *cis / trans*-Influence on Stability, Insertion Chemistry and NMR Chemical Shifts

Luca Rocchigiani,[†,*] *Julio Fernandez–Cestau* [†] *Isabelle Chambrier,* [†] *Peter Hrobárik,* [‡,§,*] *and Manfred Bochmann*[†,*]

[†] School of Chemistry, University of East Anglia, Norwich Research Park, NR4 7TJ, Norwich, United Kingdom

[‡] Institut für Chemie, Technische Universität Berlin, Straße des 17. Juni 135, D-10623 Berlin, Germany

[§] Department of Inorganic Chemistry, Faculty of Natural Sciences, Comenius University, SK-84215 Bratislava, Slovakia

l.rocchigiani@uea.ac.uk

peter.hrobarik@uniba.sk

m.bochmann@uea.ac.uk

Table of Contents

1. Relevant ^{1}H and ^{13}C NMR spectra

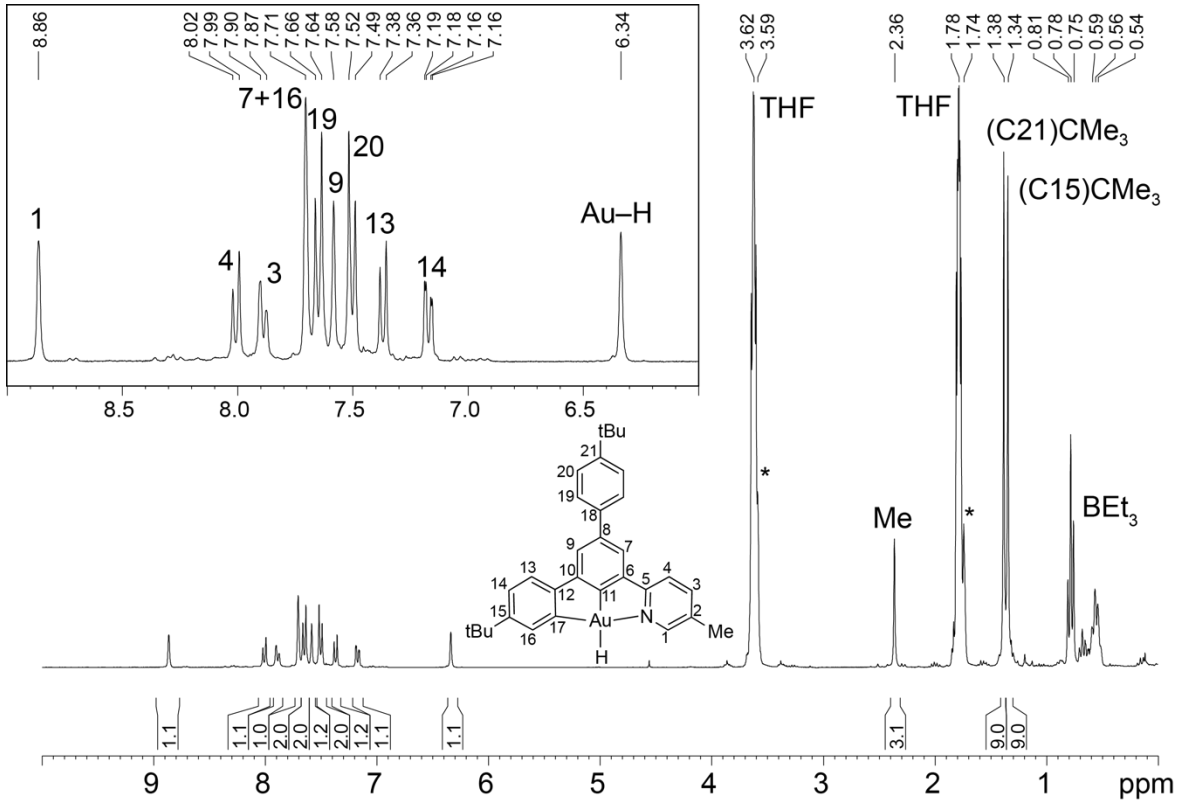

Figure S1. ^{1}H NMR spectrum of **4** (THF–d_8, 253K); * denote residual protonated THF–d_8.

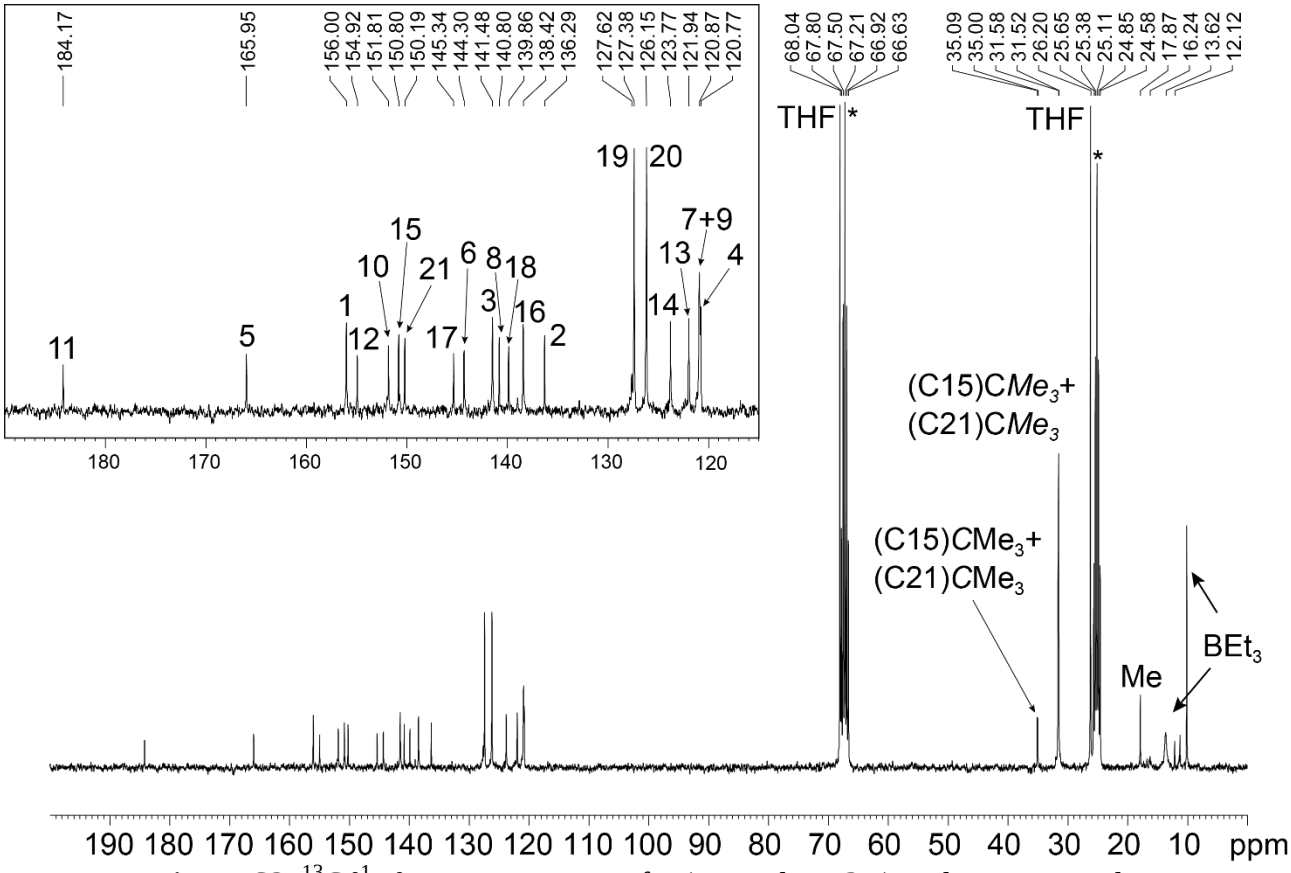

Figure S2. ^{13}C{^{1}H} NMR spectrum of **4** (THF–d_8, 253K); * denote THF–d_8.

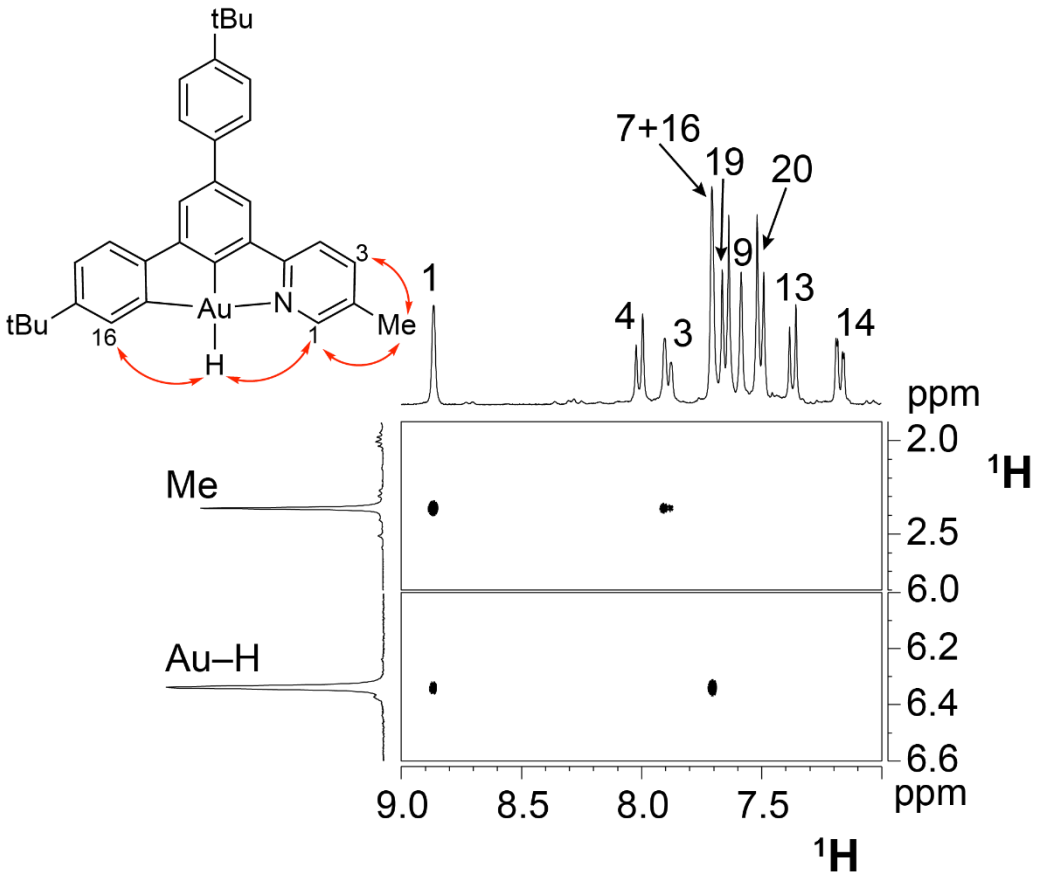

Figure S3. Two sections of the ^{1}H NOESY NMR spectrum of **4** (THF–d_8, 253K); red arrows in the scheme denote dipolar contacts.

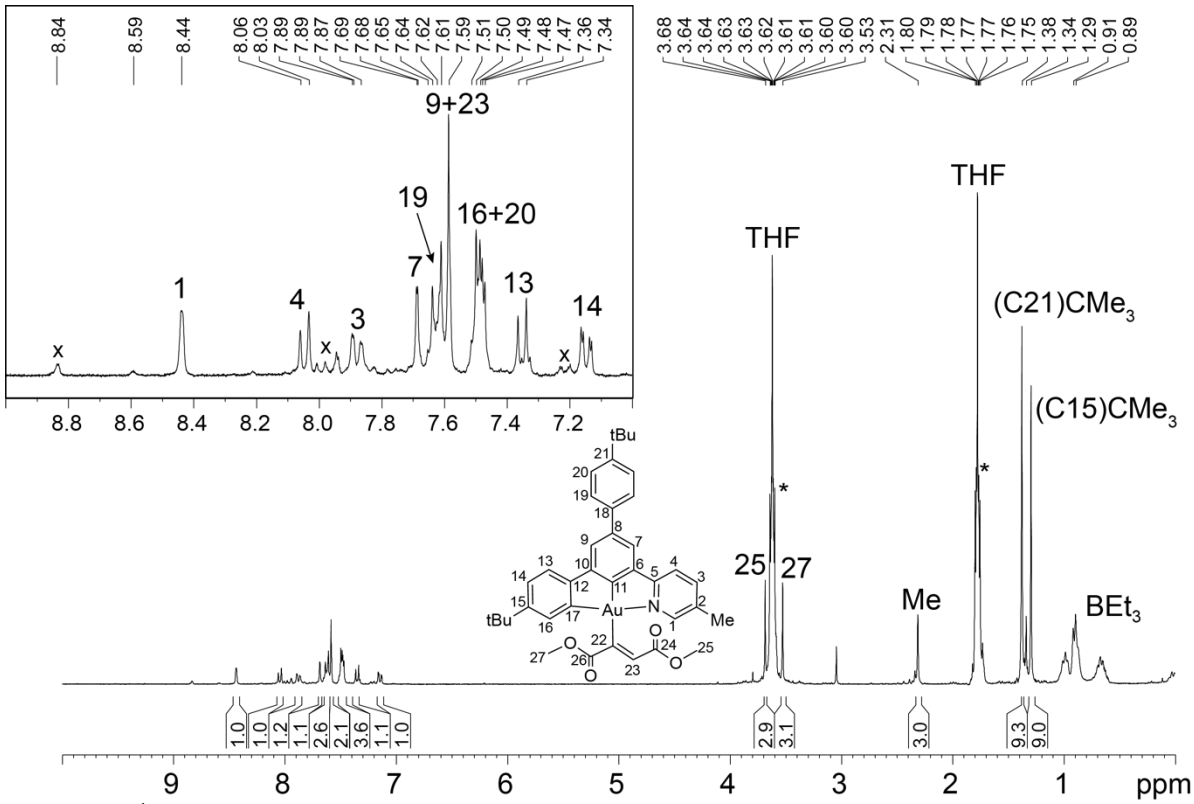

Figure S4. ^{1}H NMR spectrum of the product obtained after the reaction between **4** and DMAD (THF–d_8, 297K); x= unreacted **1**, * denote residual protonated THF–d_8.

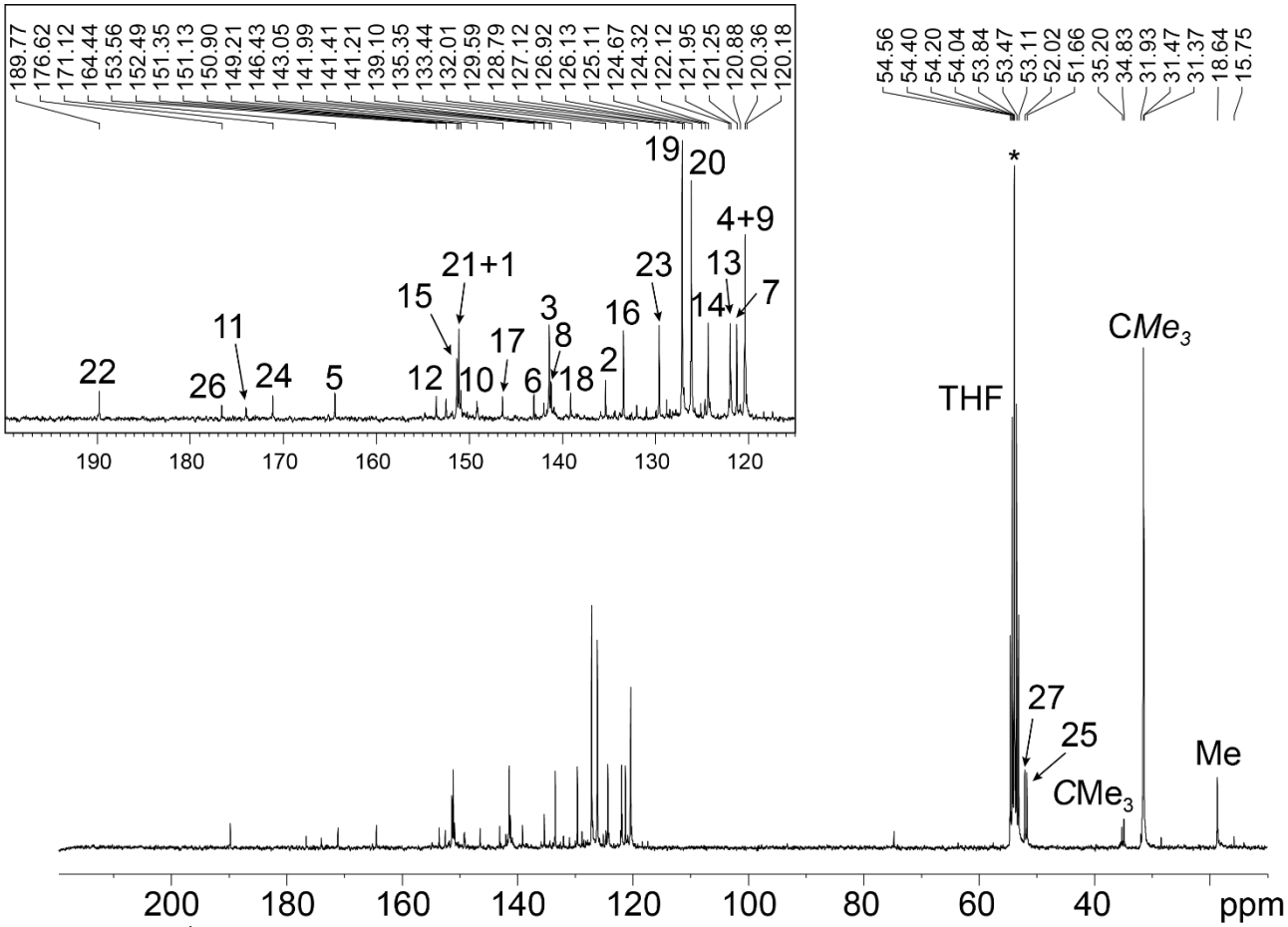

Figure S5. ^{1}H NMR spectrum of the product obtained after the reaction between **4** and DMAD (CD_2Cl_2, 297K); * denote CD_2Cl_2.

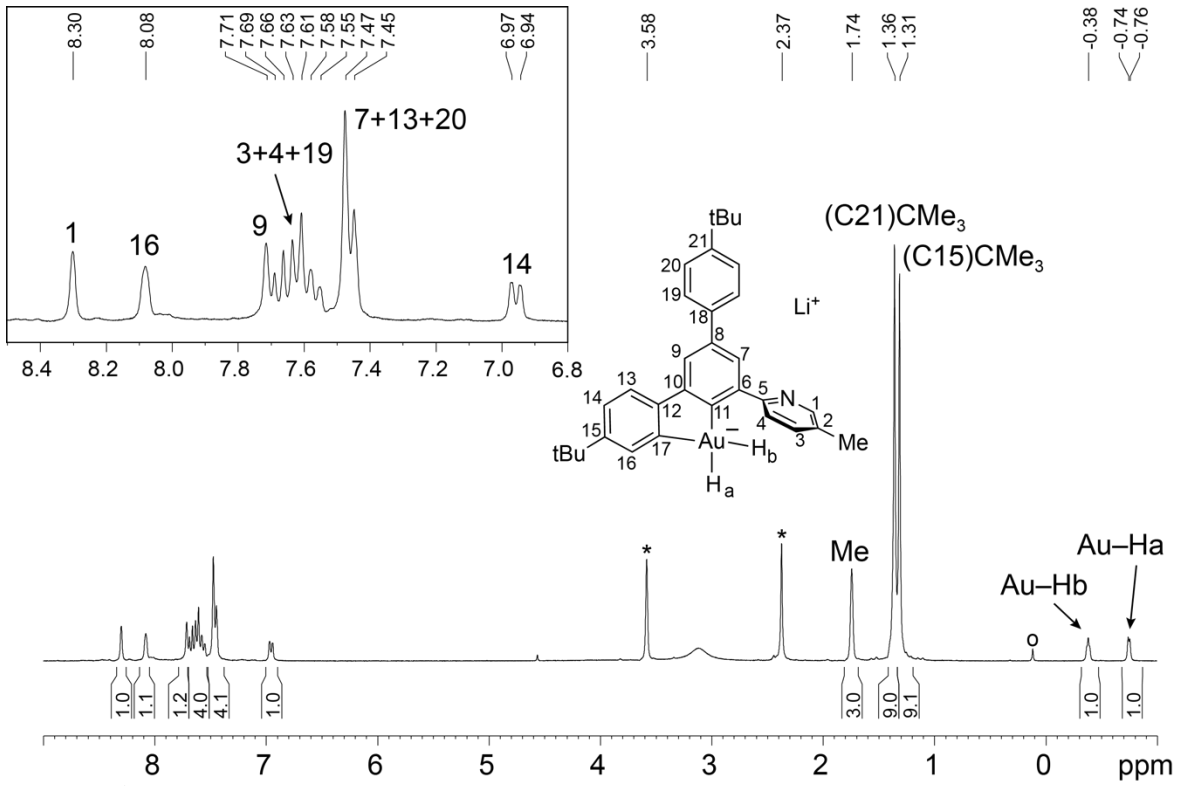

Figure S6. ^{1}H NMR of **5** obtained by procedure b (THF–d_8, 263K); * denote residual protonated THF–d_8, o denotes silicone grease.

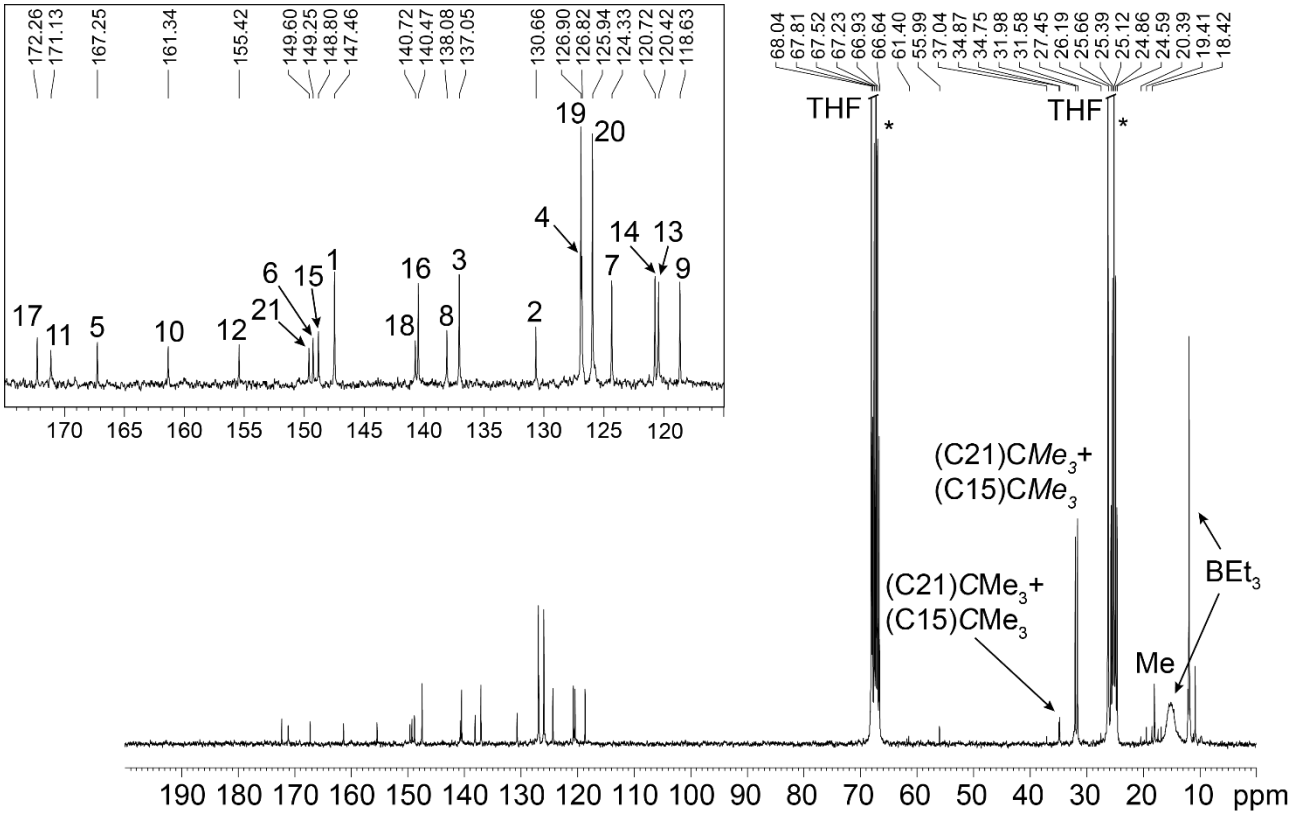

Figure S7. ^{1}H NMR of **5** obtained by procedure a (THF–d_8, 263K); * denote THF–d_8.

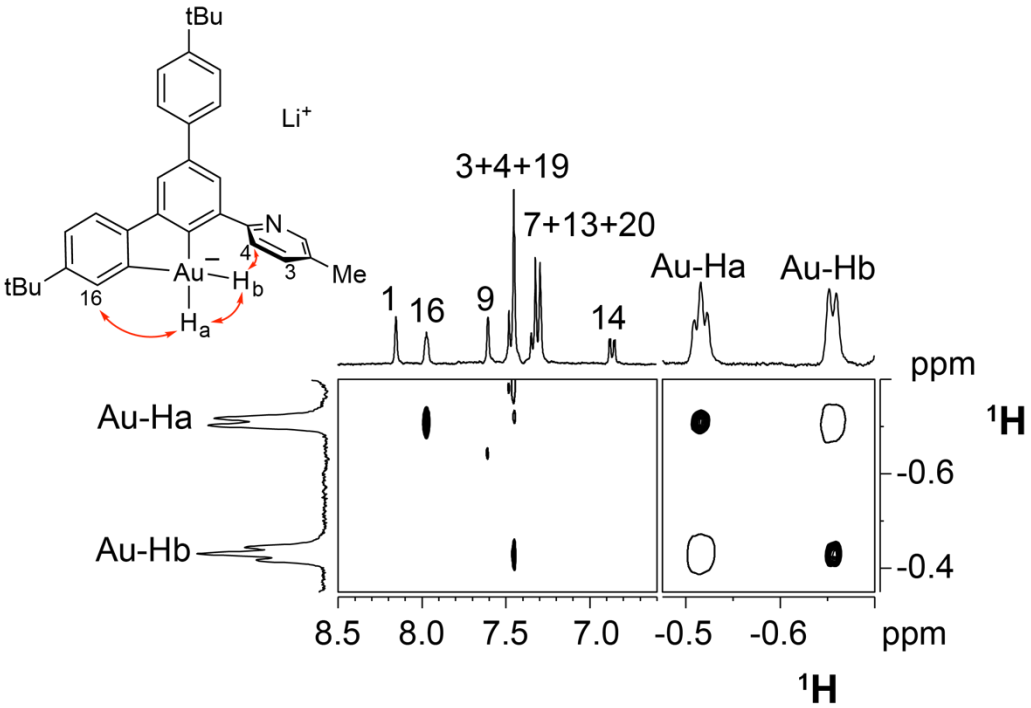

Figure S8. Two sections of the ^{1}H NOESY NMR spectrum of **5** (THF–d_8, 263K).

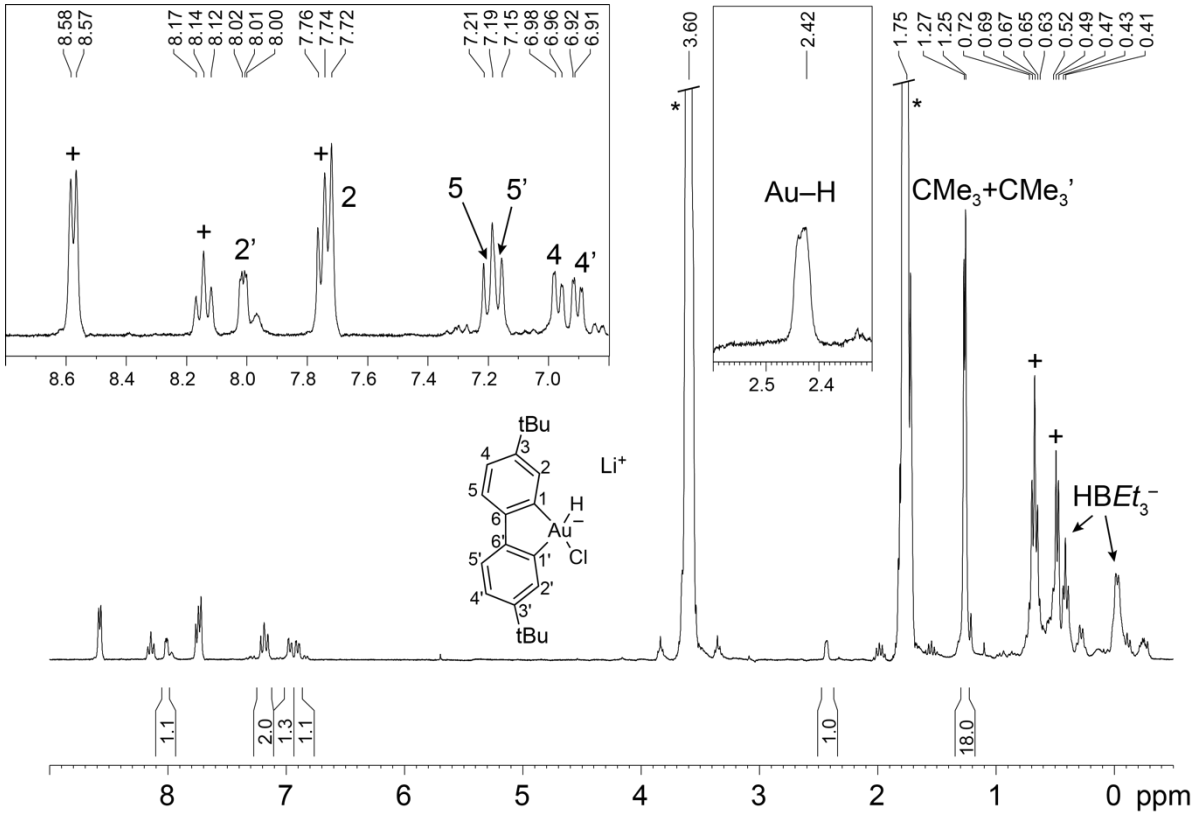

Figure S9. ^{1}H NMR of **6** (THF–d_8, 223K); * denote residual protonated THF–d_8,+: py–BEt_3.

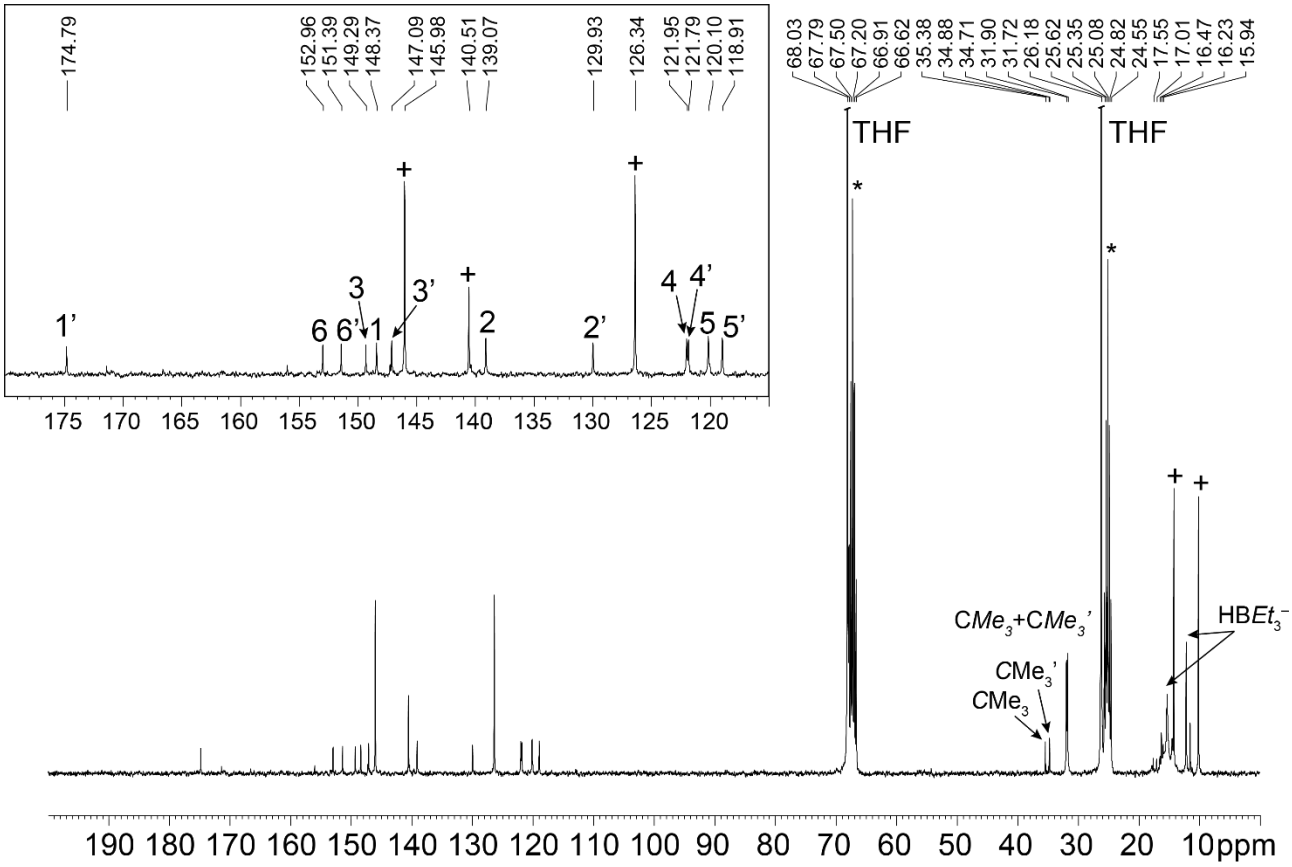

Figure S10. ^{13}C{^{1}H} NMR of **6** (THF–d_8, 223K); * denote THF–d_8,+: py–BEt_3.

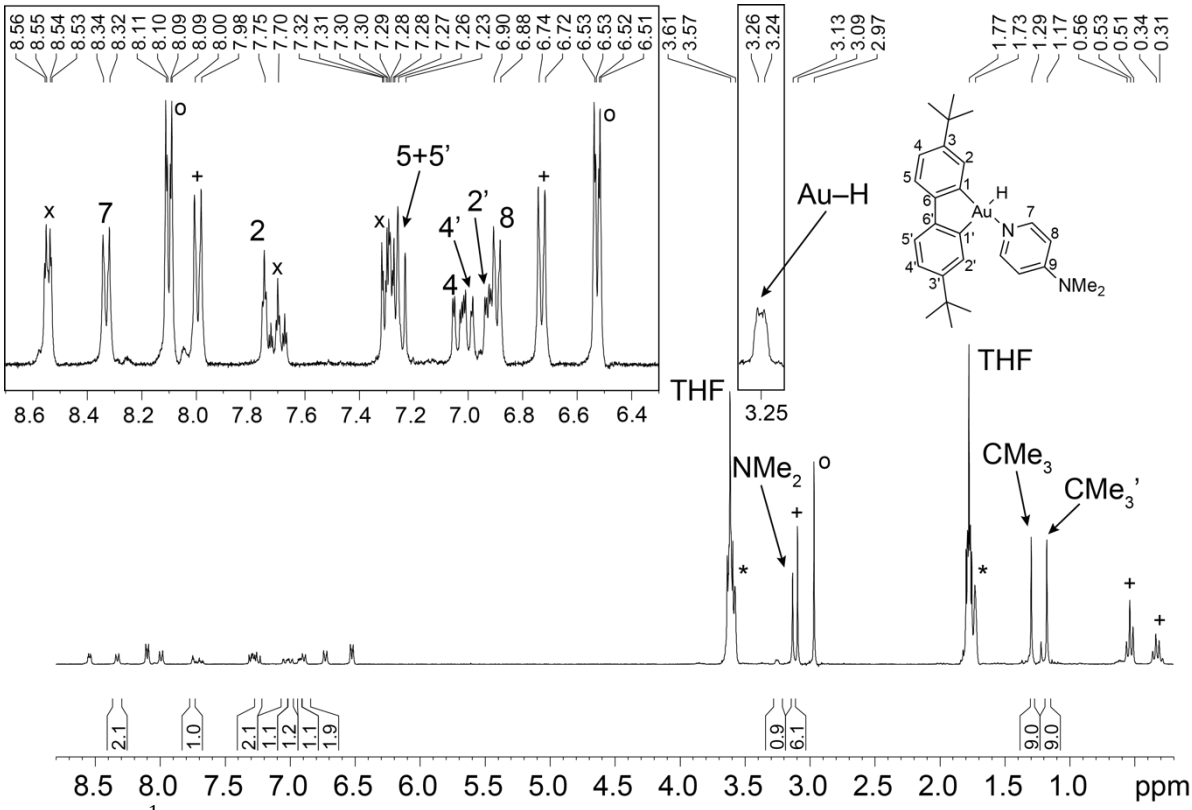

Figure S11. ^{1}H NMR of **7** (THF–d_8, 253K); * = residual protonated THF–d_8,+:DMAP–BEt_3, x: pyridine, o: free DMAP.

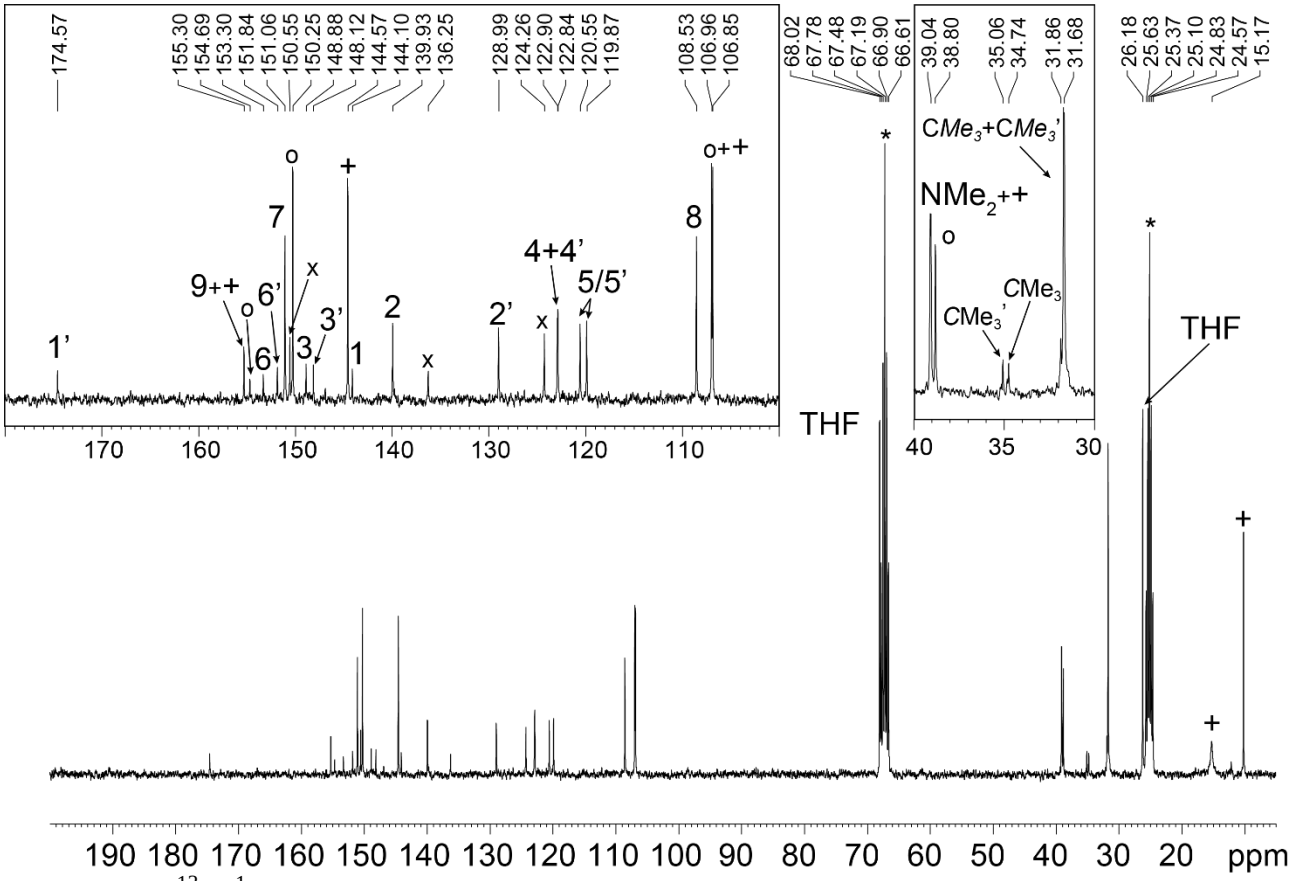

Figure S12. ^{13}C{^{1}H} NMR of **7** (THF–d_8, 253K); * = THF–d_8,+: DMAP–BEt_3, x: pyridine, o: free DMAP.

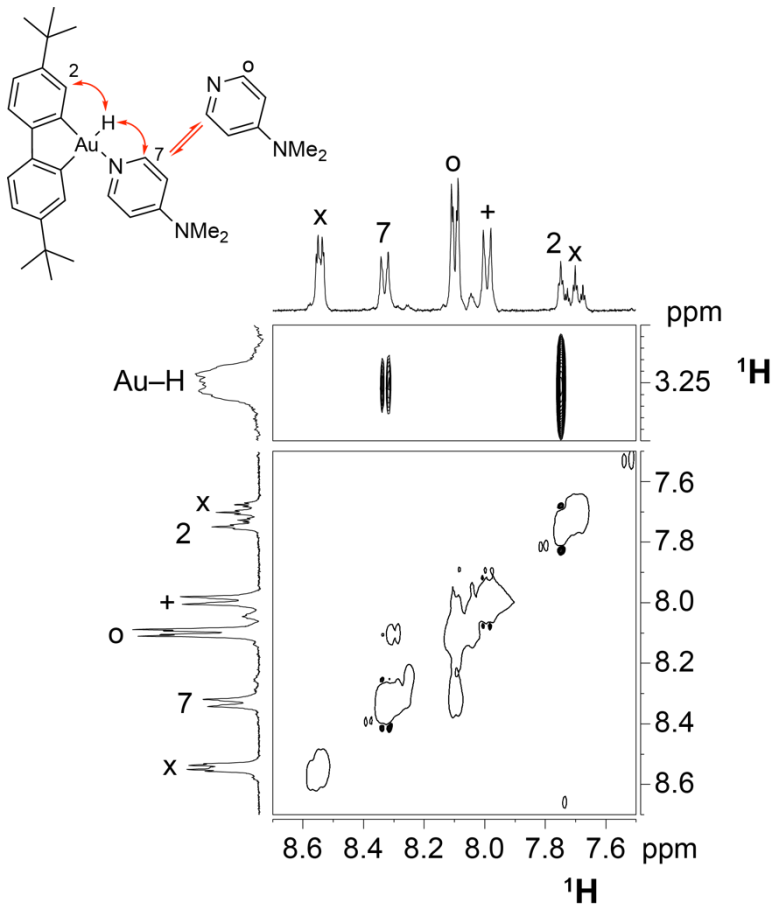

Figure S13. Two sections of the ^{1}H NOESY NMR spectrum of **7** (THF–d_8, 253K); +: DMAP–BEt_3, x: pyridine, o: free DMAP.

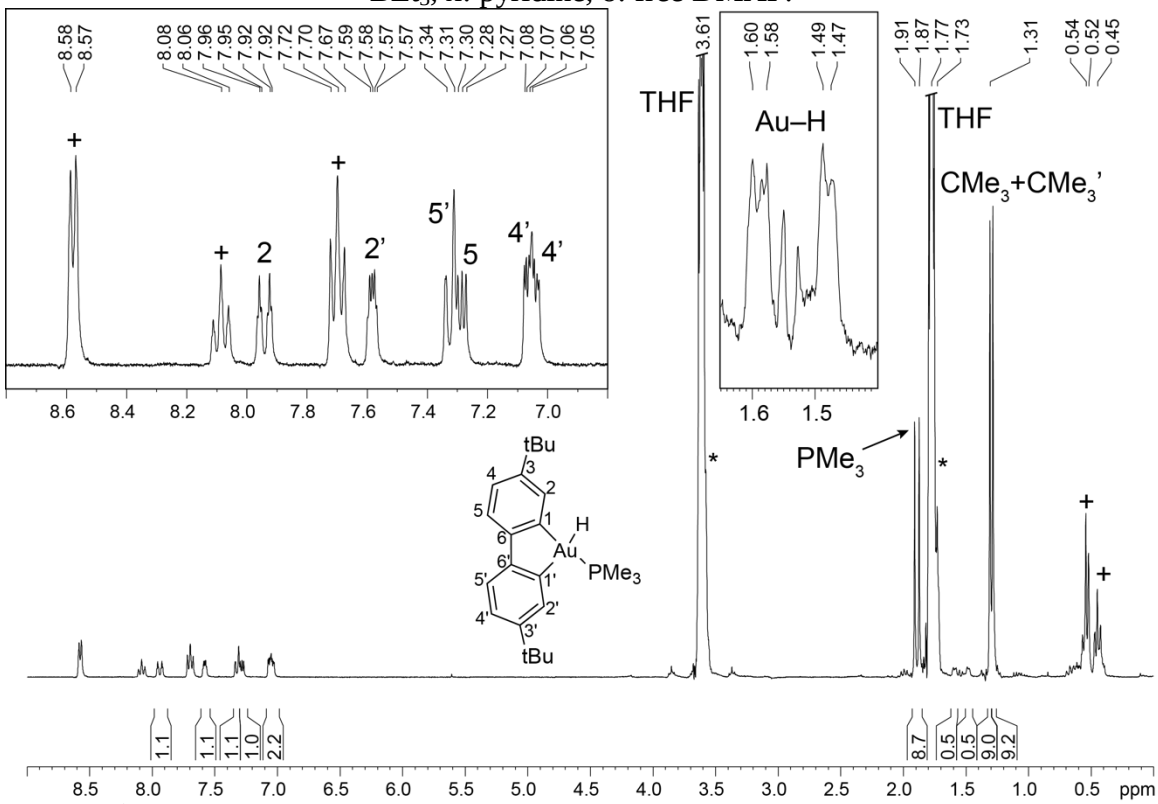

Figure S14. ^{1}H NMR of **9** obtained by procedure a (THF–d_8, 263K); * denote residual protonated THF–d_8, +:py–BEt_3.

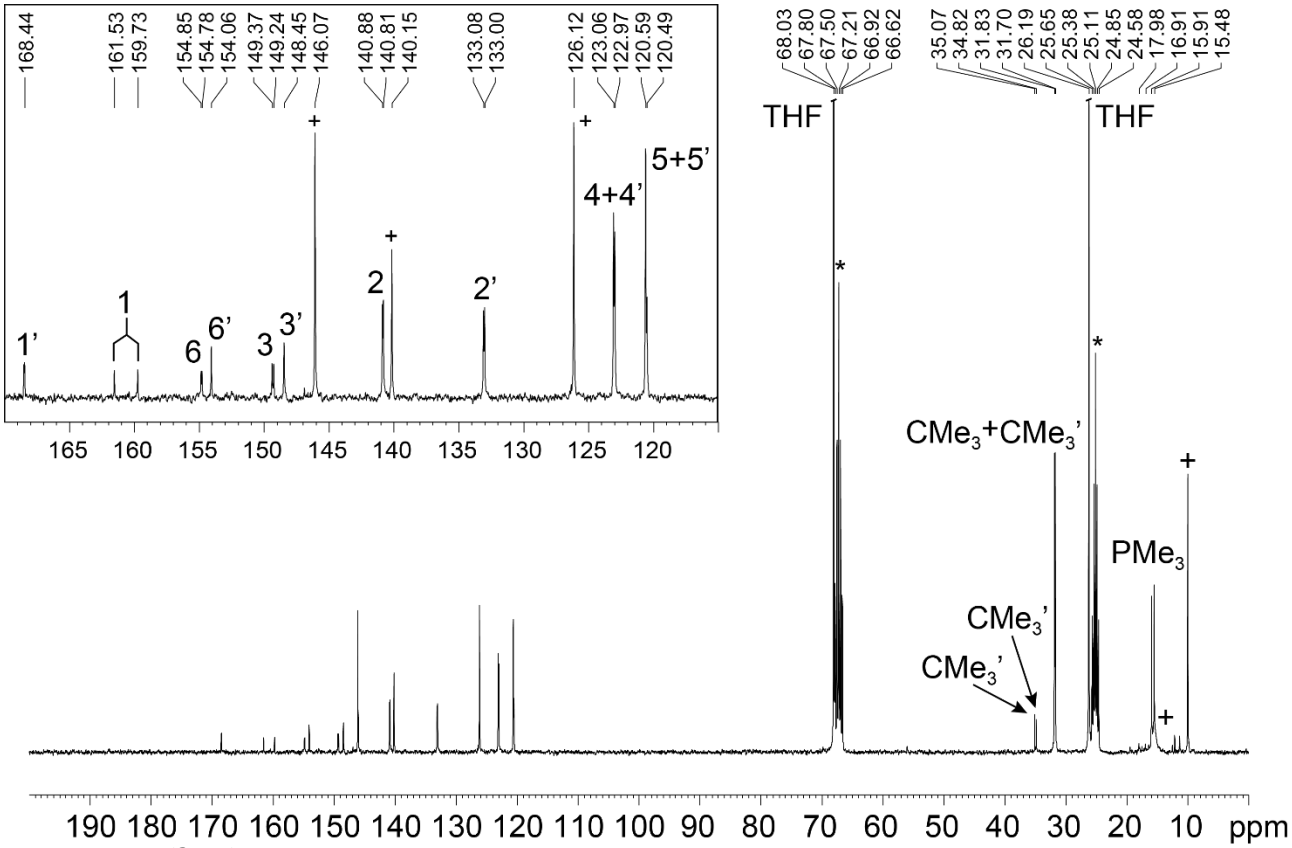

Figure S15. $^{13}C\{^{1}H\}$ NMR of **9** obtained by procedure a (THF–d_8, 263K); * denote THF–d_8, +: py–BEt_3.

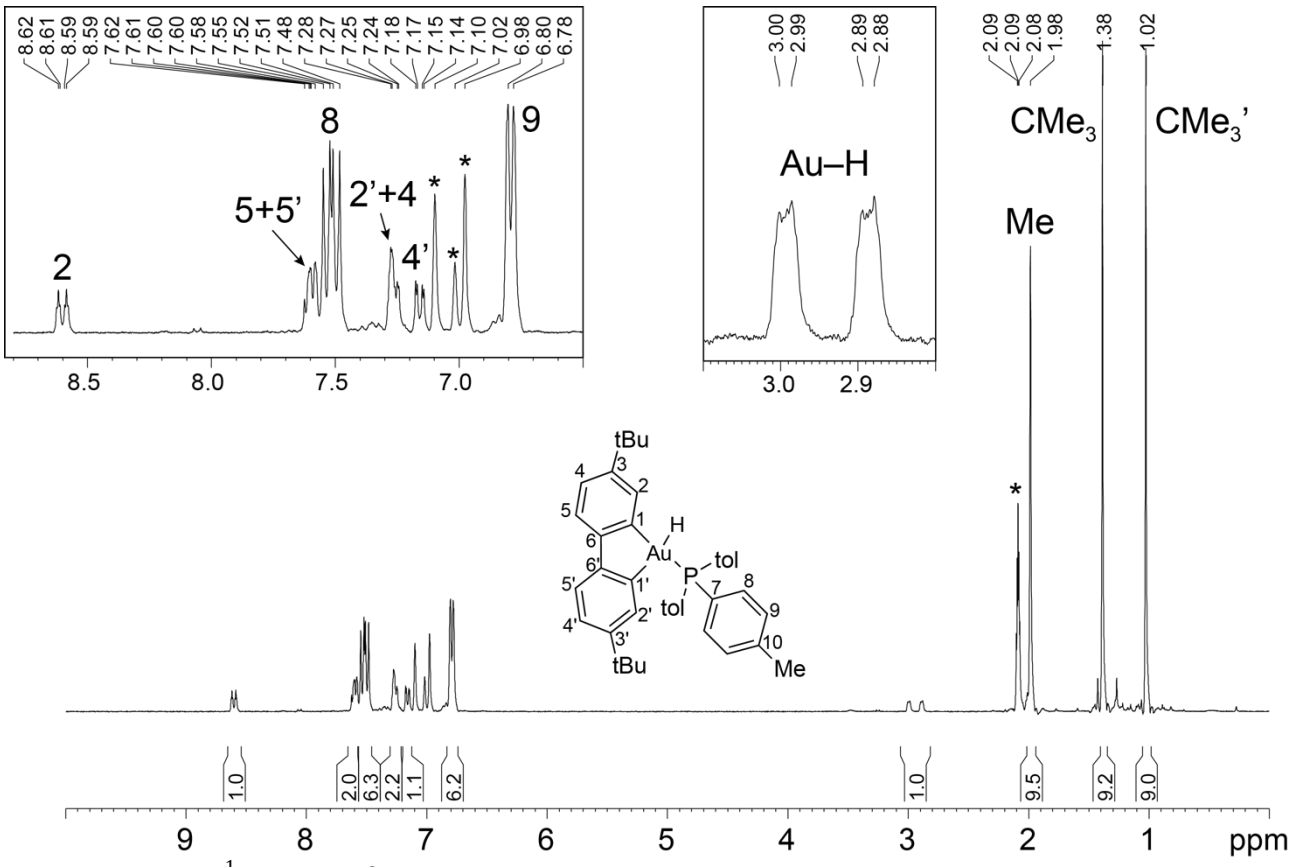

Figure S16. ^{1}H NMR of **10** obtained by procedure b (toluene–d_8, 297 K); * denote residual protonated toluene–d_8.

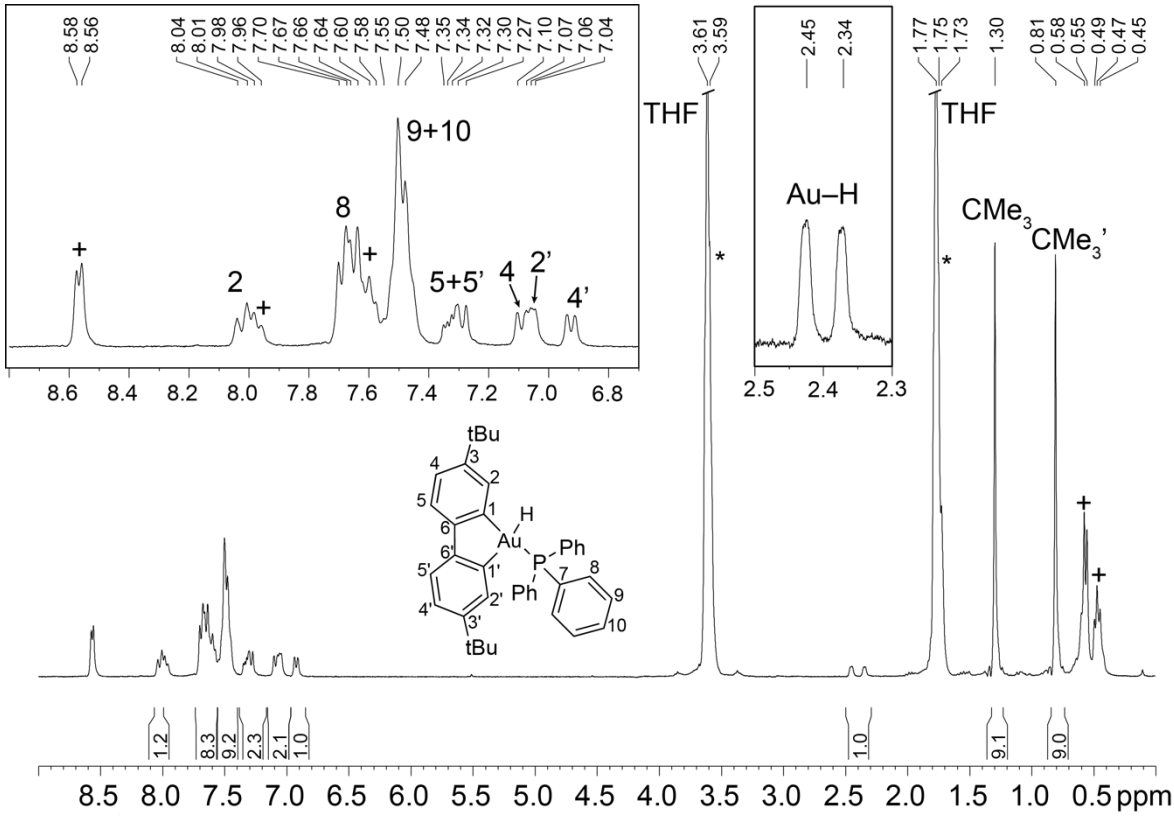

Figure S17. ^{1}H NMR of **11** obtained by procedure a (THF–d_8, 297 K); * denote residual protonated THF–d_8, + = py–BEt_3.

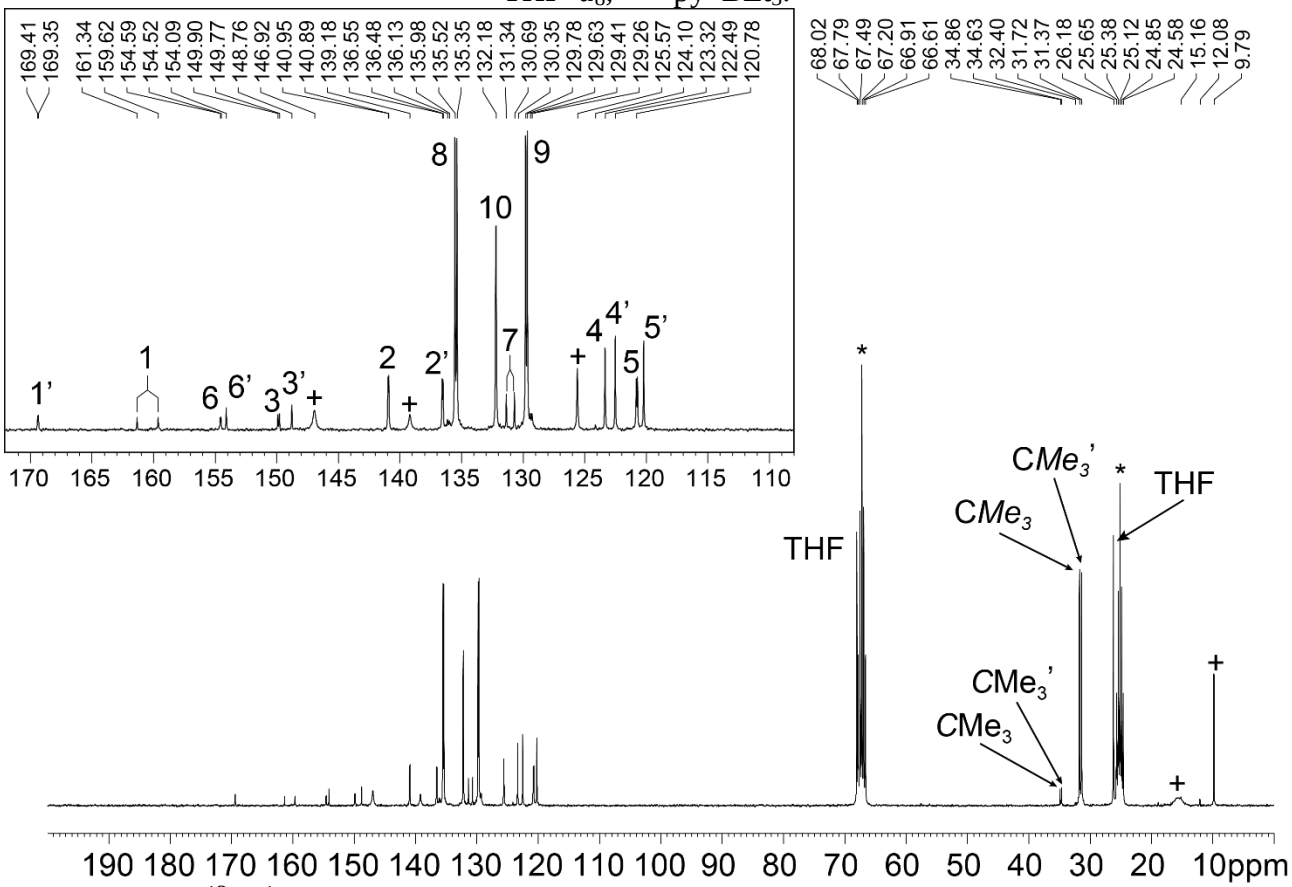

Figure S18. ^{13}C{^{1}H} NMR of **11** obtained by procedure a (THF–d_8, 297 K); * denote residual protonated THF–d_8, + = py–BEt_3.

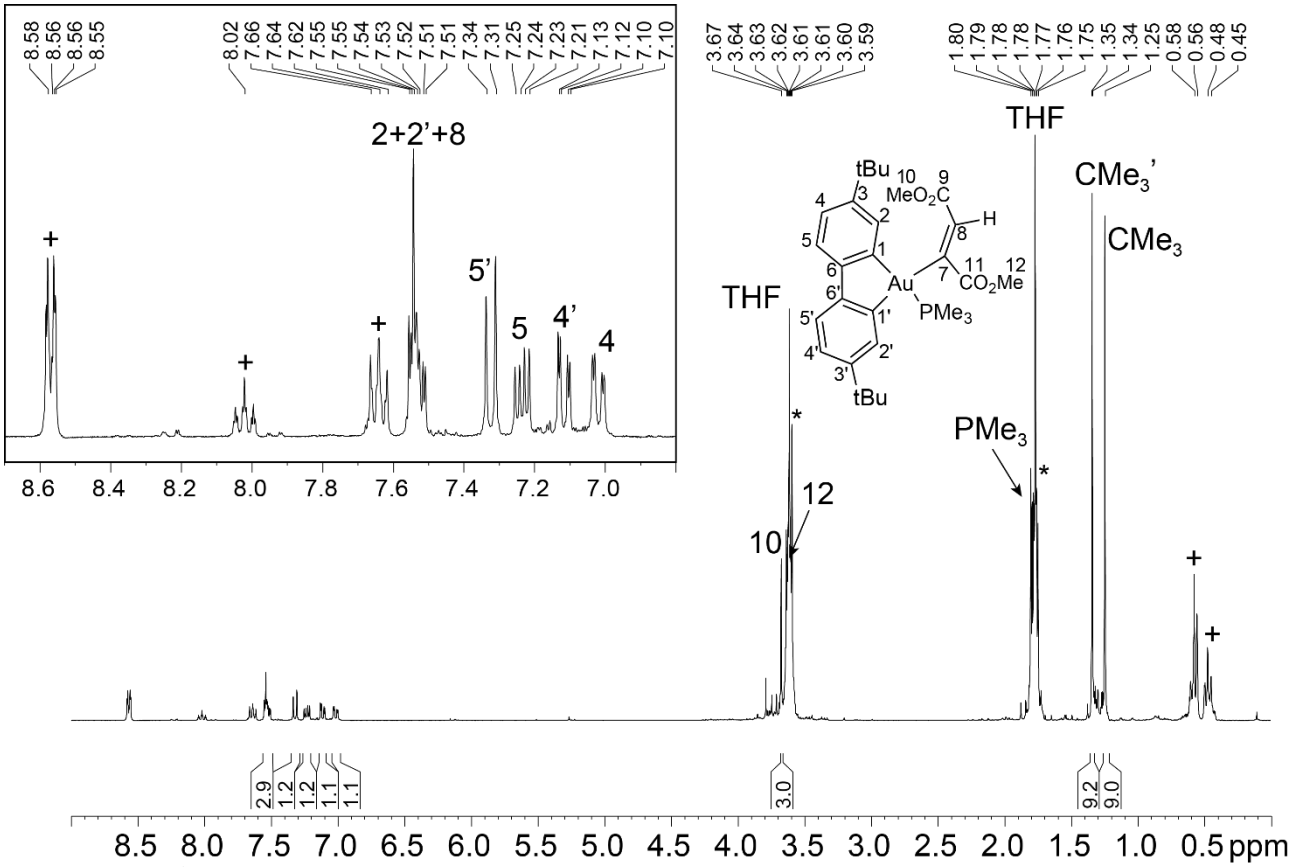

Figure S19. ^{1}H NMR of **12** generated *in situ* (THF–d_8, 297 K); * denote residual protonated THF–d_8, + = py–BEt_3.

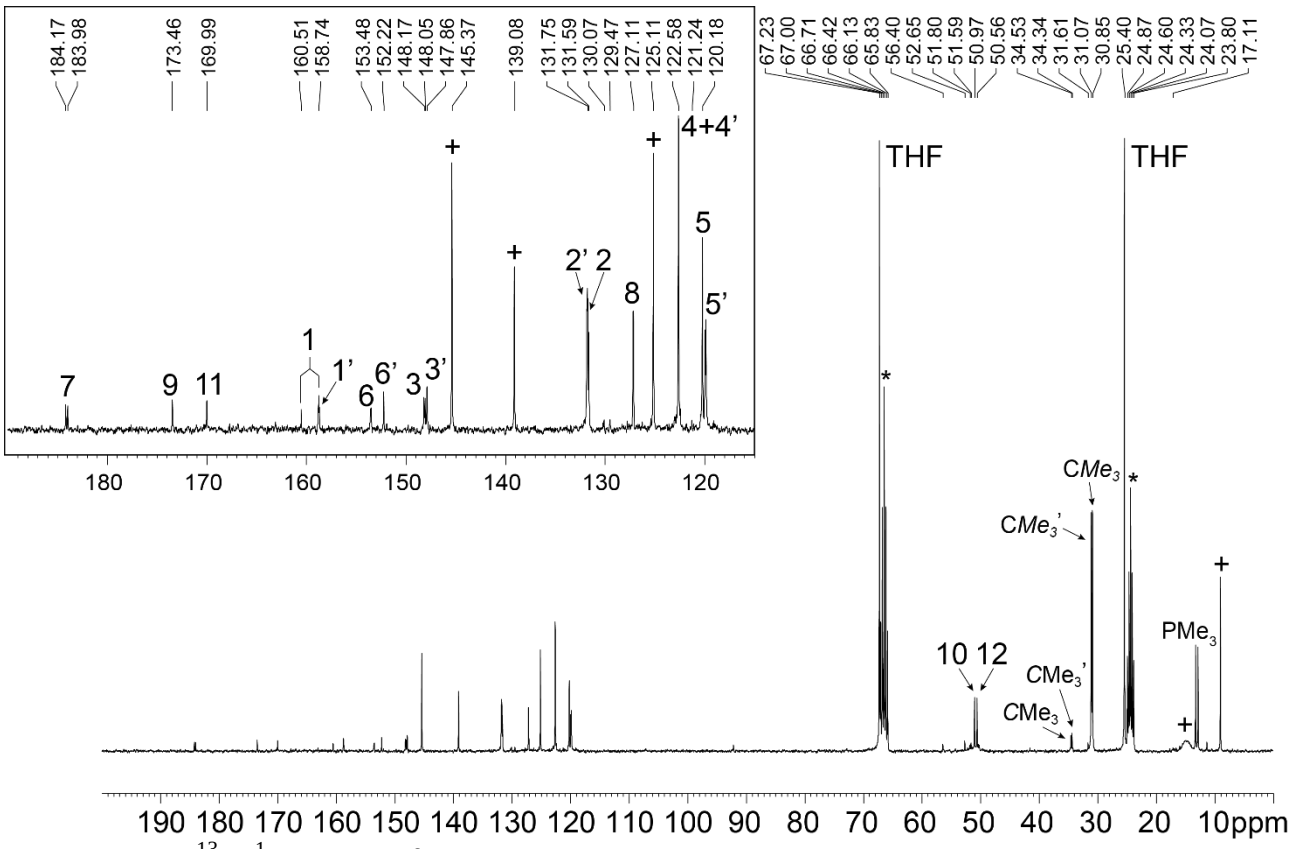

Figure S20. ^{13}C{^{1}H} NMR of **12** generated *in situ* (THF–d_8, 297 K); * denote THF–d_8, + = py–BEt_3.

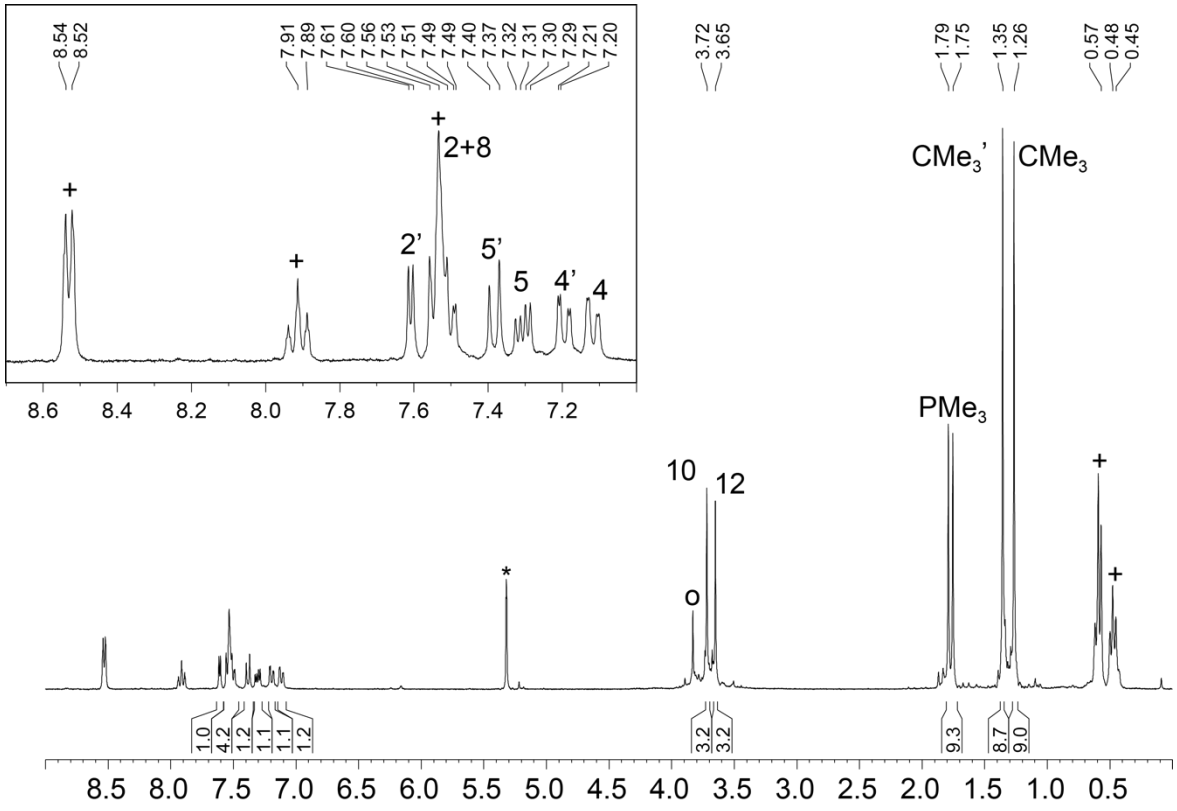

Figure S21. ^{1}H NMR of **12** generated *in situ* (CD_2Cl_2, 297 K); * denote residual protonated deuterated solvent, + = py–BEt_3, o=DMAD residue.

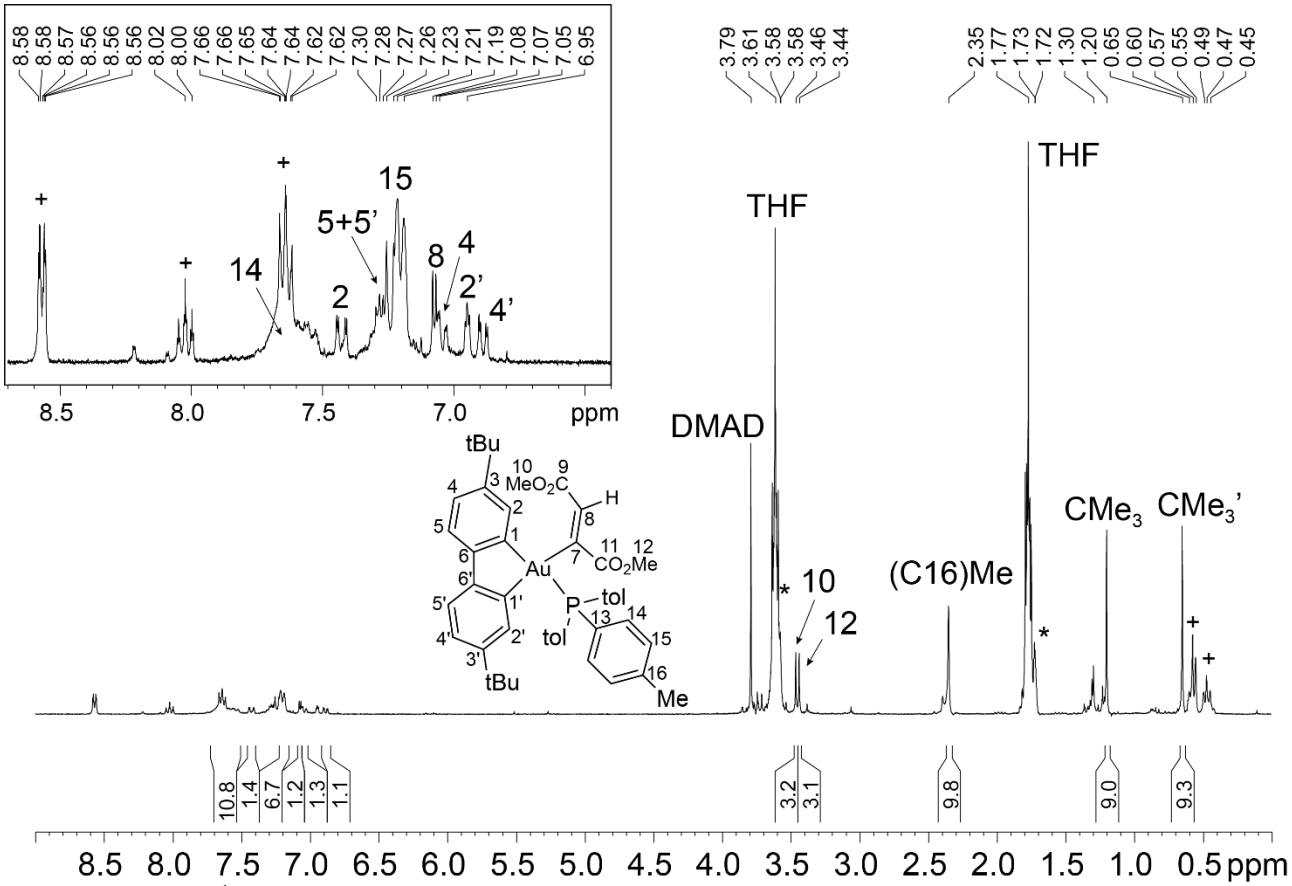

Figure S22. ^{1}H NMR of **13** generated *in situ* (THF–d_8, 297 K); * denote residual protonated deuterated solvent, + = py–BEt_3.

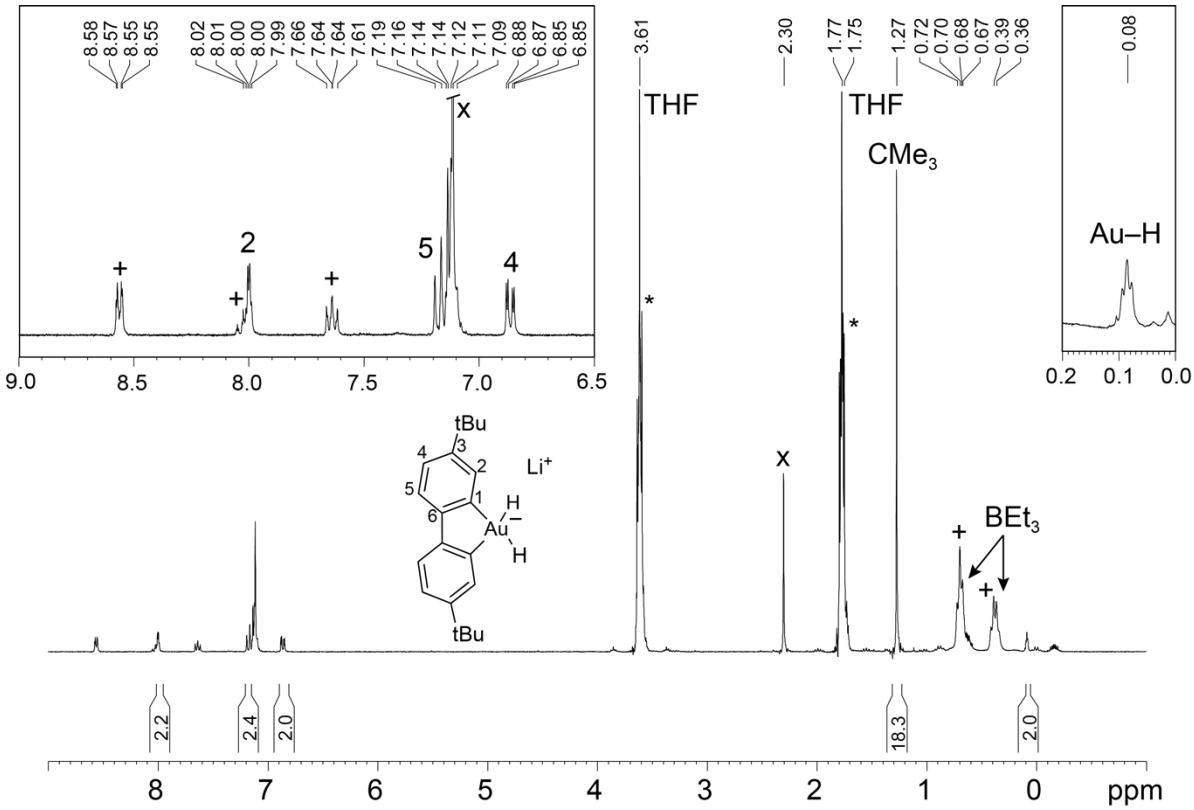

Figure S23. ^{1}H NMR spectrum of **14** (THF–d_8, 297K); * denote residual protonated THF–d_8, + = py–BEt_3, x = free P(p-tol)$_3$.

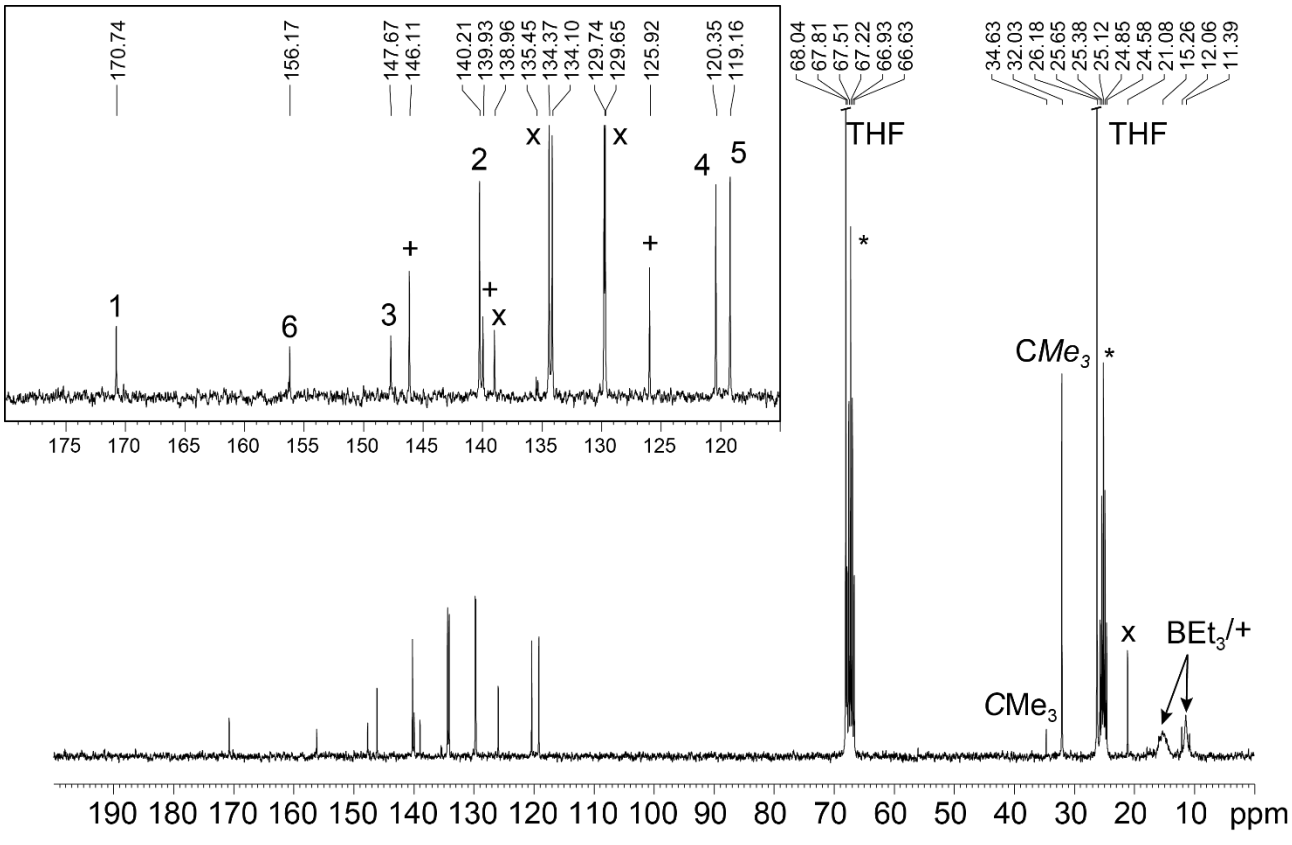

Figure S24. ^{1}H NMR spectrum of **14** (THF–d_8, 297K); * denote THF–d_8, + = py–BEt_3, x = free P(p-tol)$_3$.

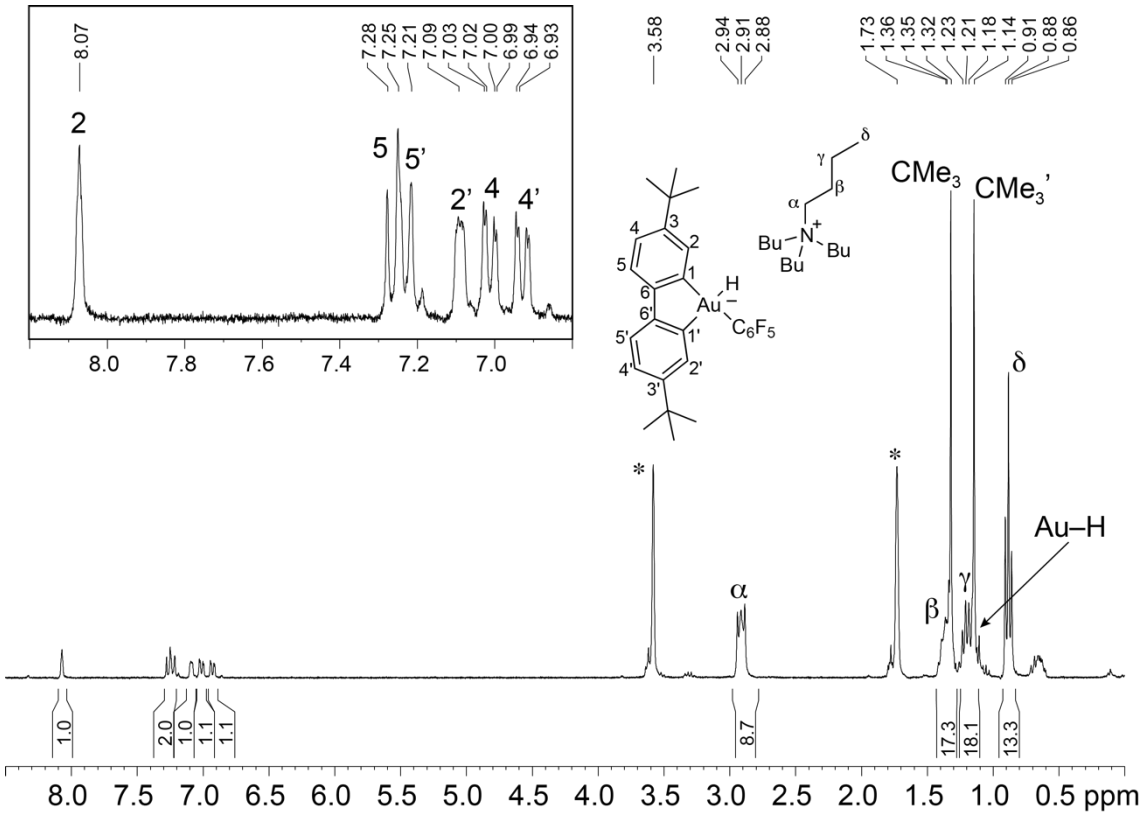

Figure S25. ^{1}H NMR spectrum of **16** (THF–d_8, 297K); * denote residual protonated THF–d_8.

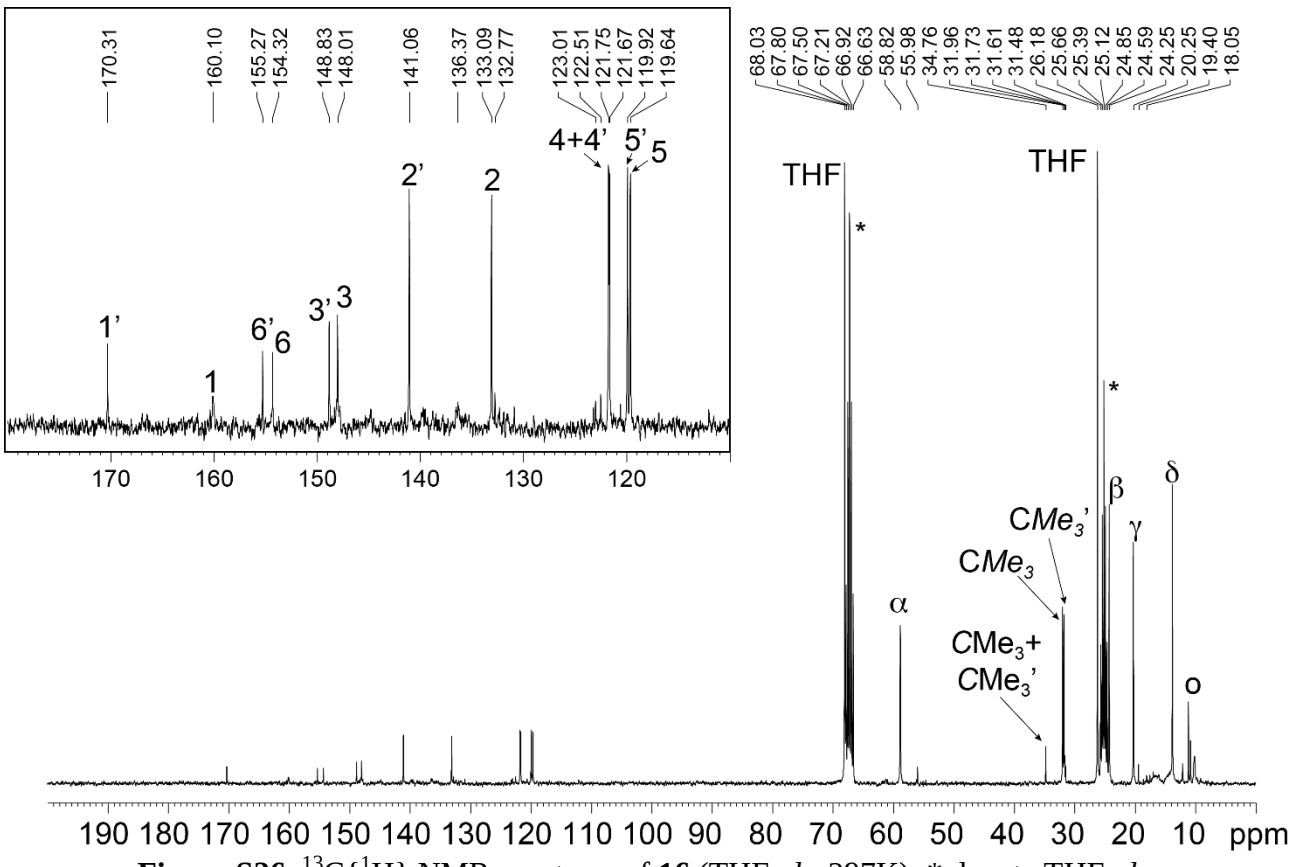

Figure S26. ^{13}C{^{1}H} NMR spectrum of **16** (THF–d_8, 297K); * denote THF–d_8.

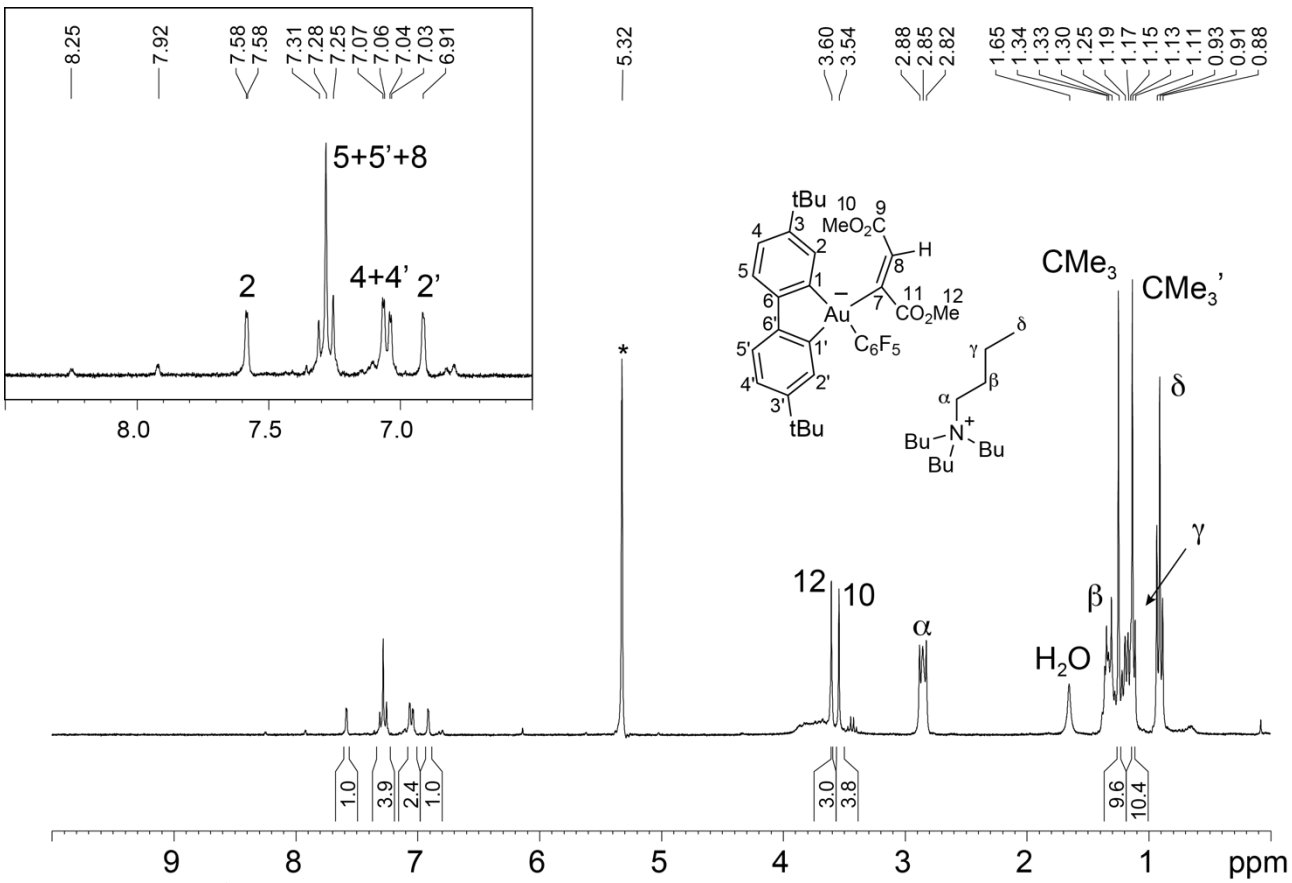

Figure S27. ^{1}H NMR spectrum of **17** (CD_2Cl_2, 297K); * denote residual protonated solvent.

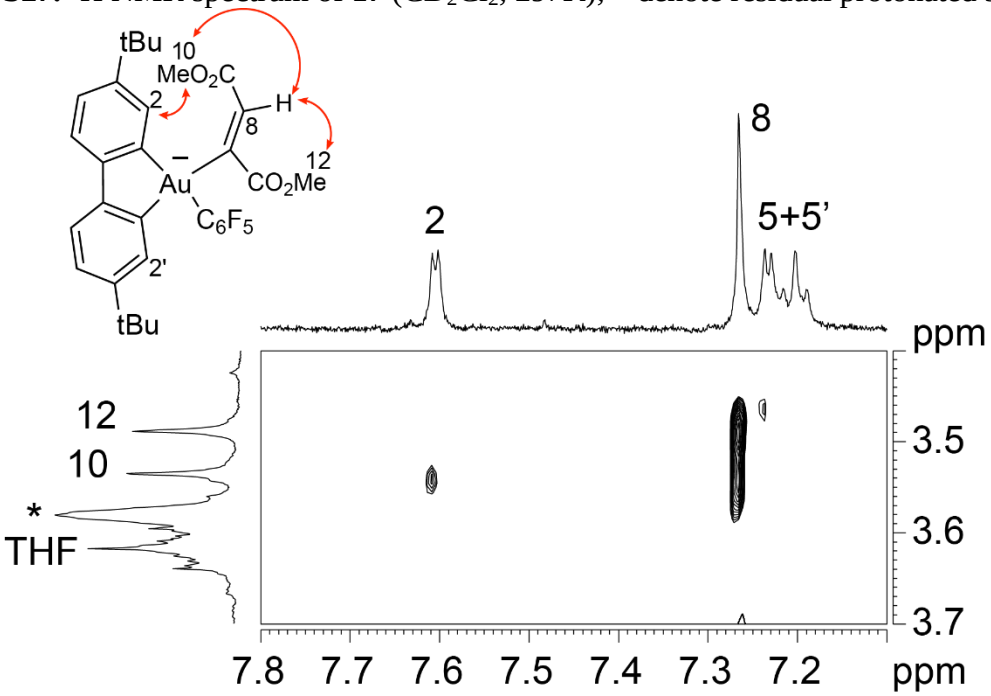

Figure S28. A section of the ^{1}H NMR spectrum of **17** (THF–d_8, 297K); * denote residual protonated solvent.

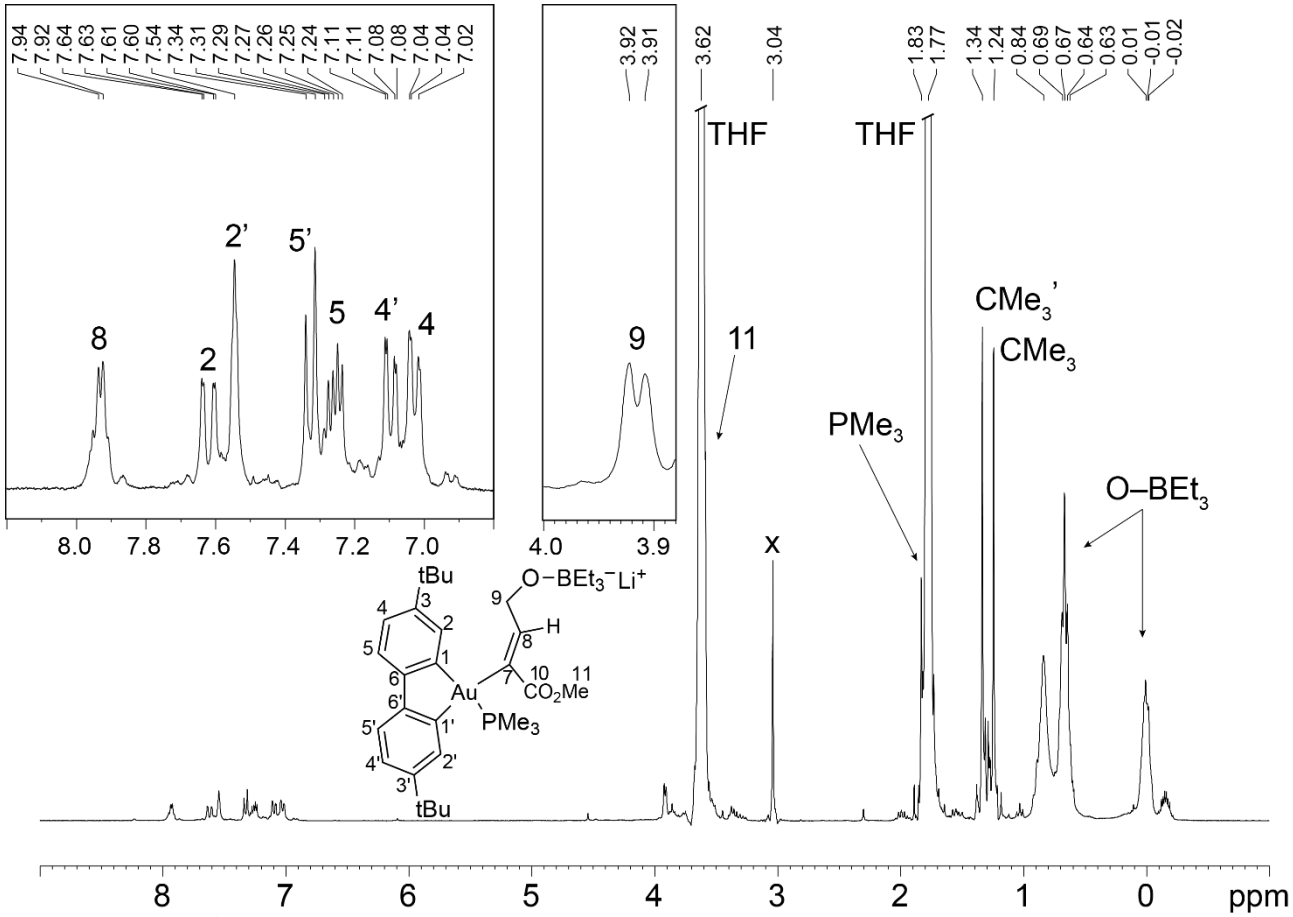

Figure S29. ^{1}H NMR of **18** (THF–d_8, 297K); x is assigned to Li[MeO–BEt_3] formed after the reduction.

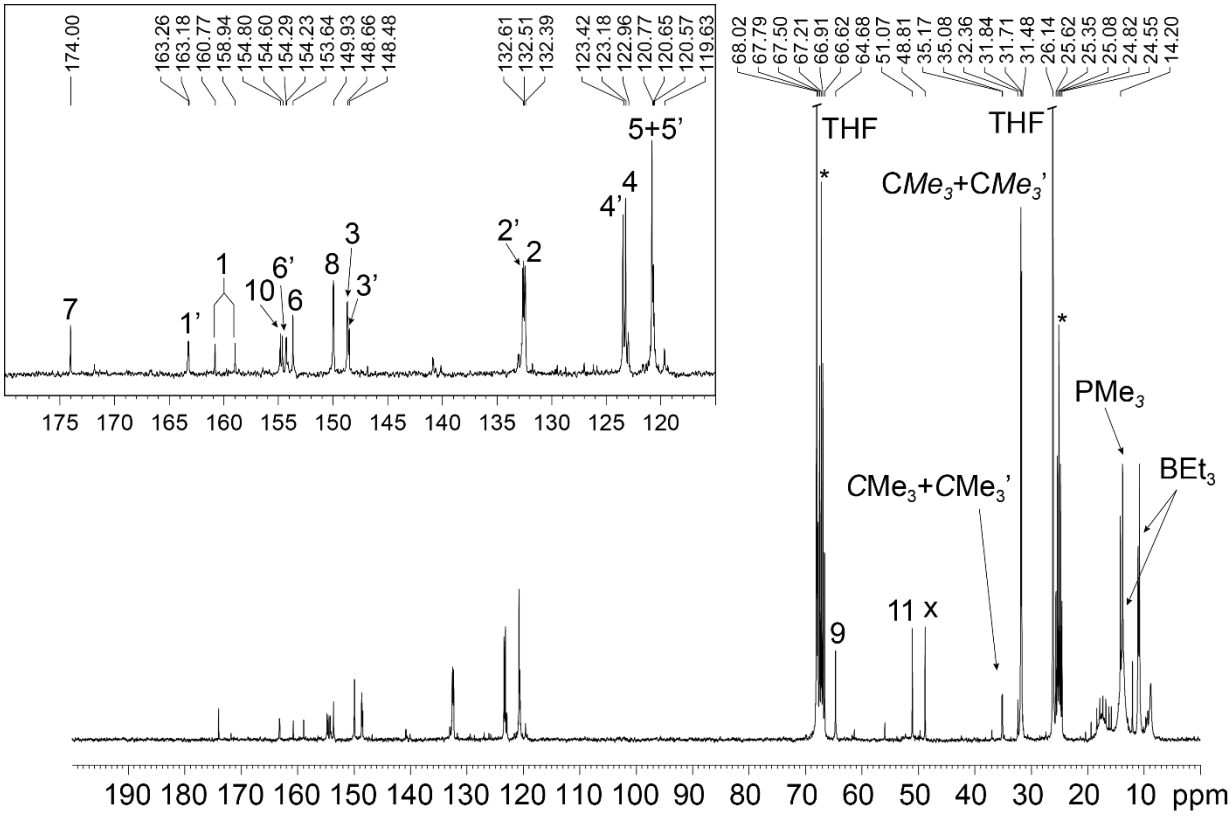

Figure S30. ^{13}C{^{1}H} NMR of **18** (THF–d_8, 297K); x is assigned to Li[MeO–BEt_3] formed after the reduction. * denote THF–d_8.

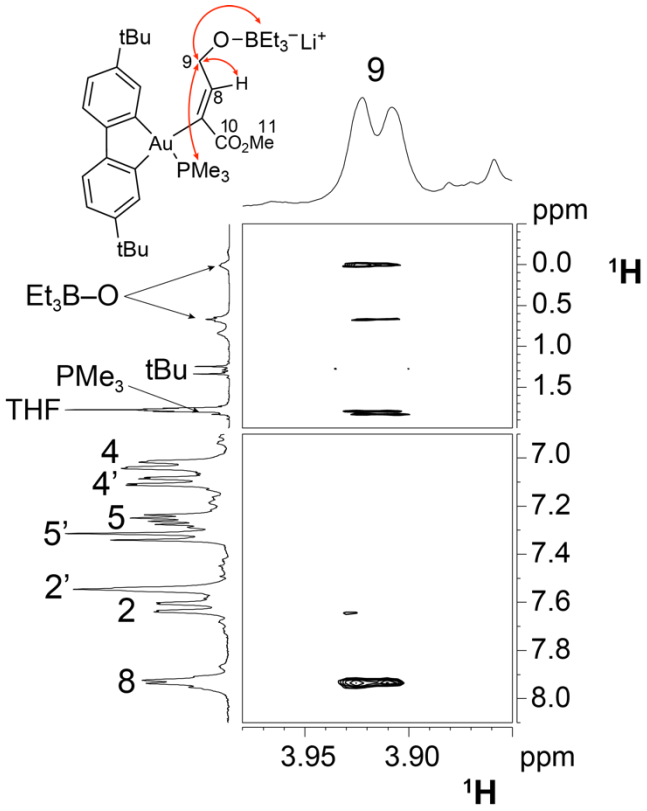

Figure S31. Two sections of the ^{1}H NOESY NMR of **18** (THF–d_8, 297K).

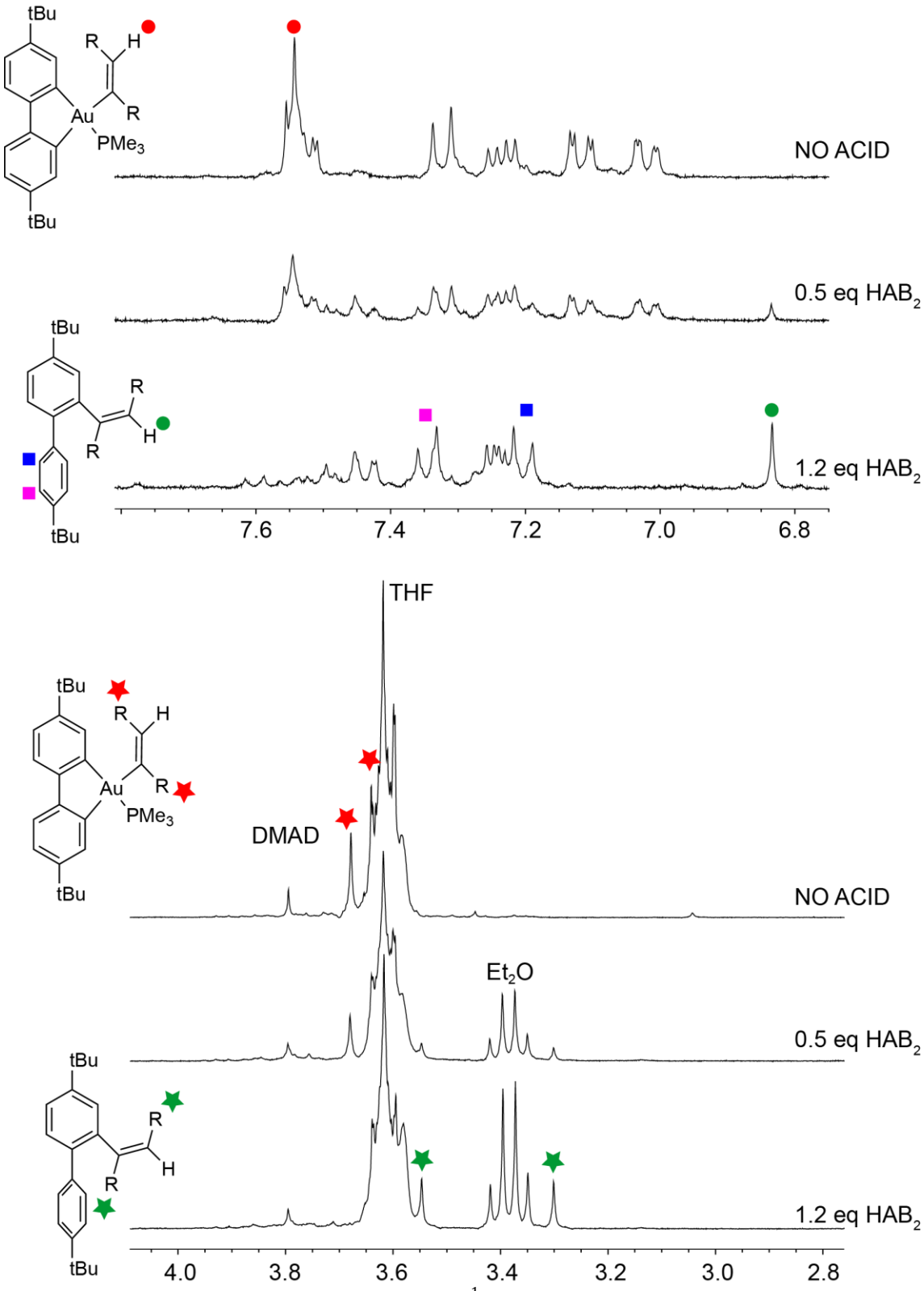

Figure S32. Evolution of two sections of the ^{1}H NMR spectrum of **12** upon reaction with $[H(OEt_2)_2][H_2N\{B(C_6F_5)_3\}_2]$ (HAB_2) at 297K in THF–d_8.

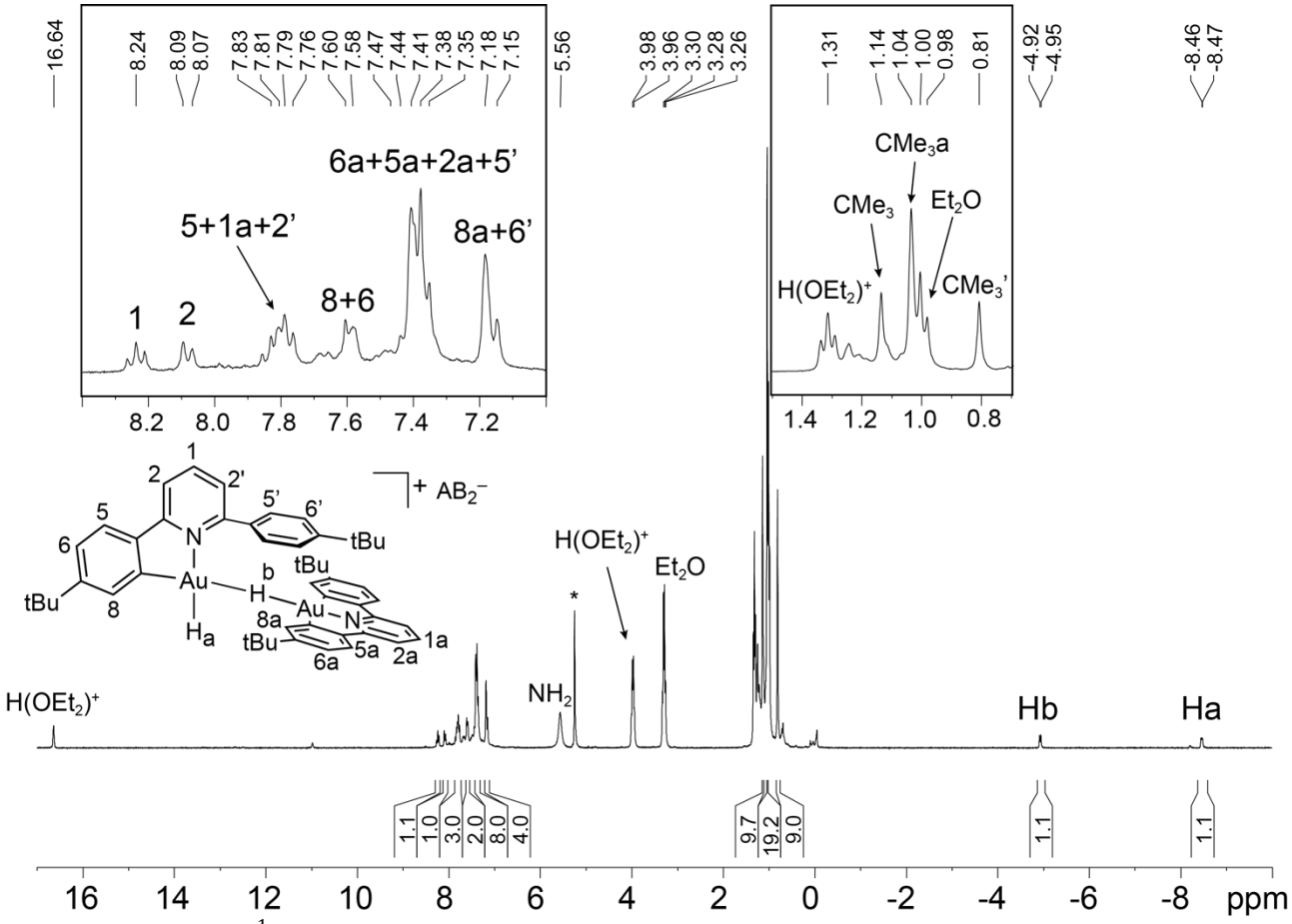

Figure S33. ^{1}H NMR obtained after the reaction of (C^N^C)AuH with 1 equivalent of $[H(OEt_2)_2][H_2N\{B(C_6F_5)_3\}_2]$ (CD_2Cl_2, 213K); * denotes residual protonated CD_2Cl_2.

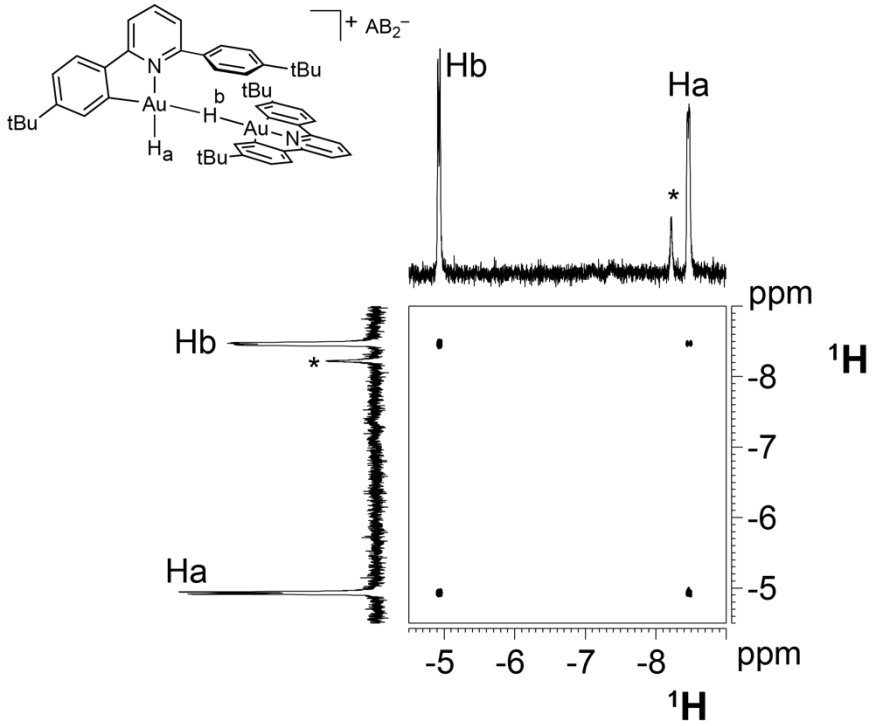

Figure S34. ^{1}H COSY NMR spectrum of complex **20** (CD_2Cl_2, 213K); * denotes side product.

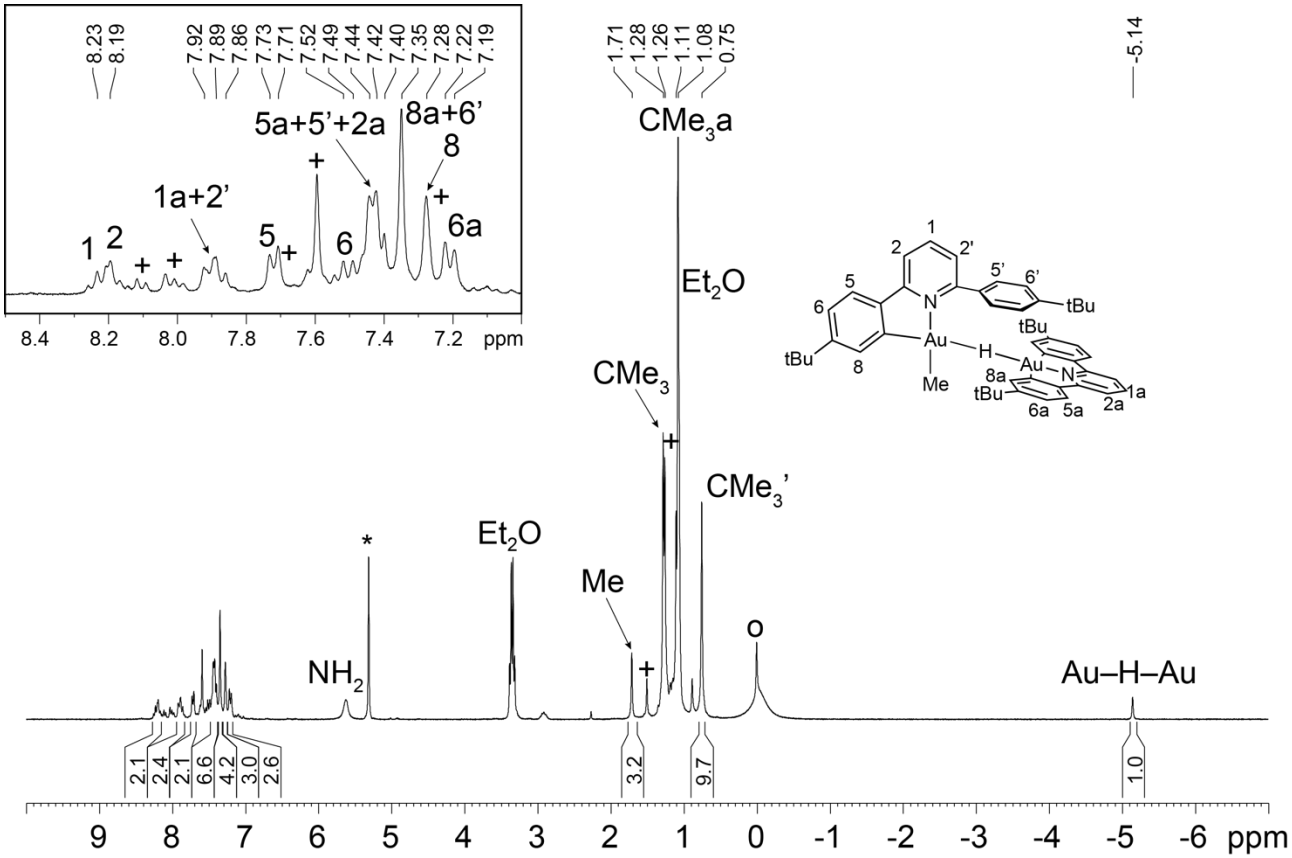

Figure S35. ^{1}H NMR spectrum of complex **21** (213K, CD_2Cl_2); * denotes residual protonated CD_2Cl_2, o denotes silicone grease, += unreacted **3a**.

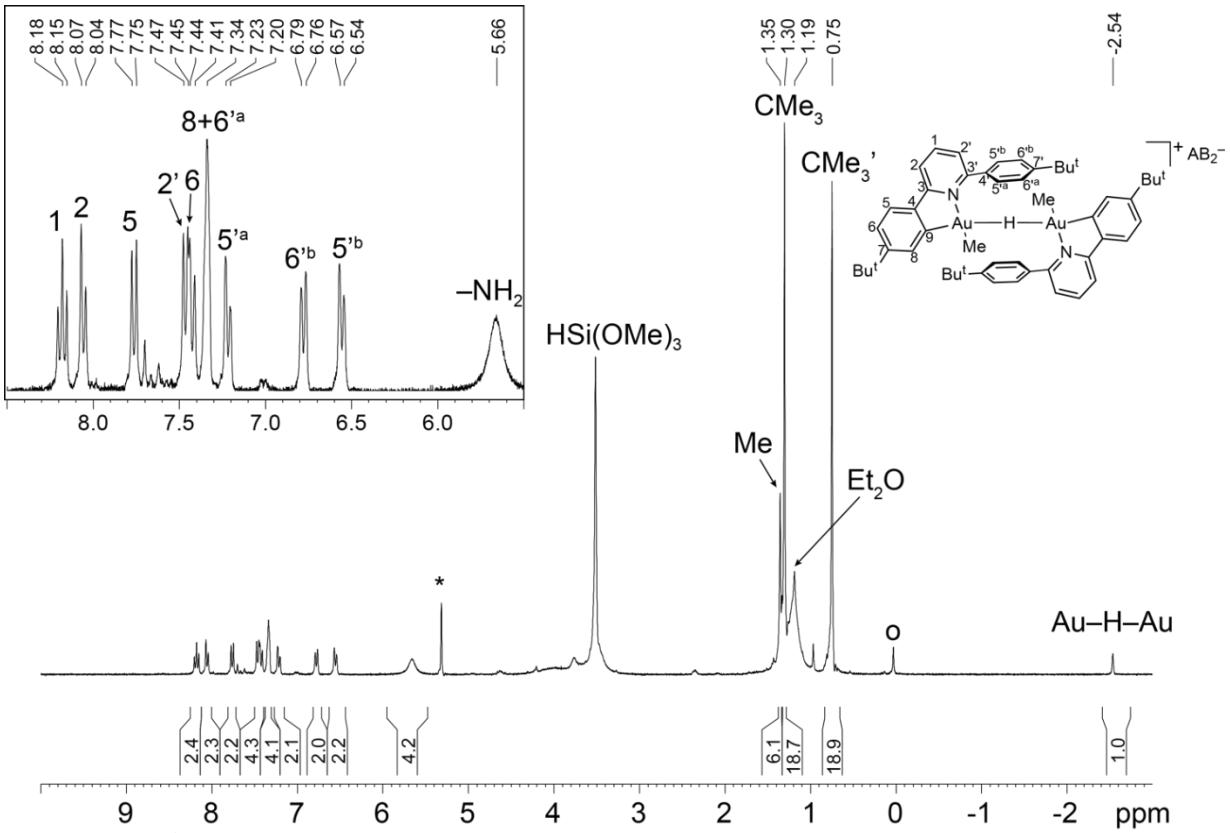

Figure S36. ^{1}H NMR spectrum of complex **22a** (253K, CD_2Cl_2); * denotes residual protonated CD_2Cl_2, o denotes silicone grease.

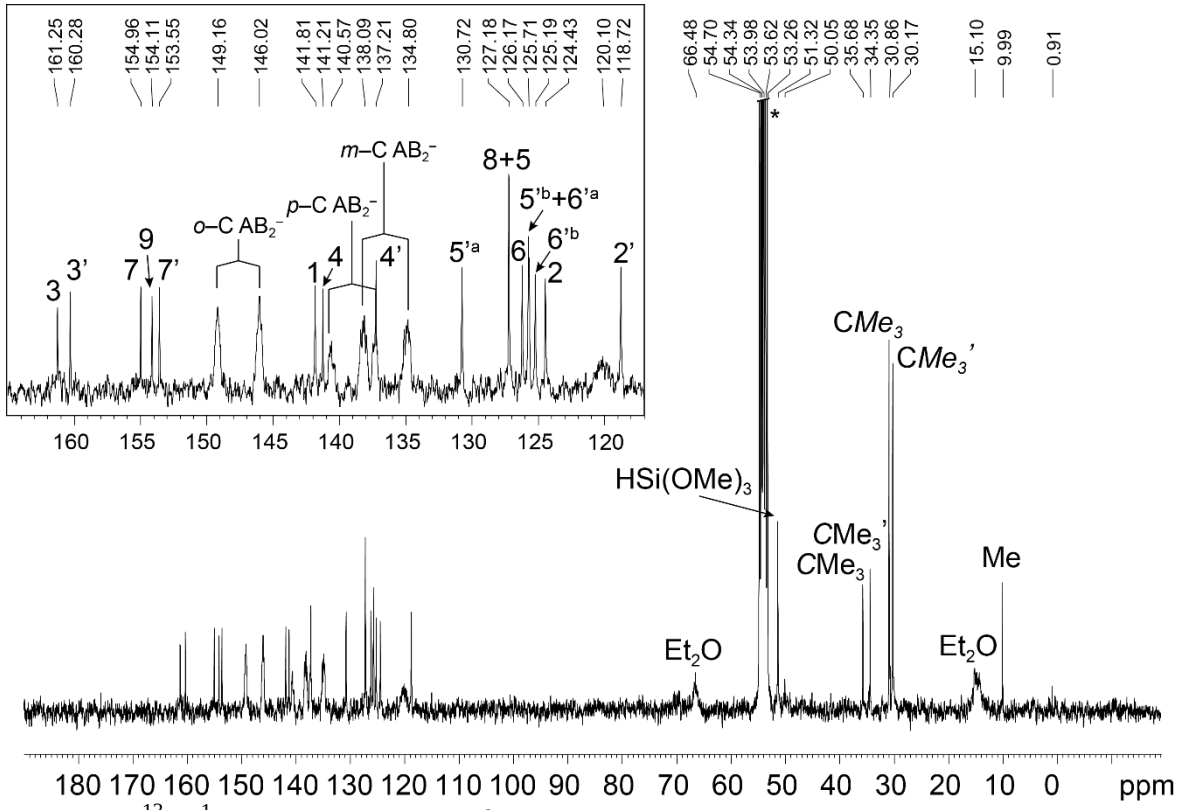

Figure S37. $^{13}C\{^{1}H\}$ NMR spectrum of complex **22a** (253K, CD_2Cl_2); * denotes CD_2Cl_2; AB_2^- $=H_2N[B(C_6F_5)_3]_2^-$.

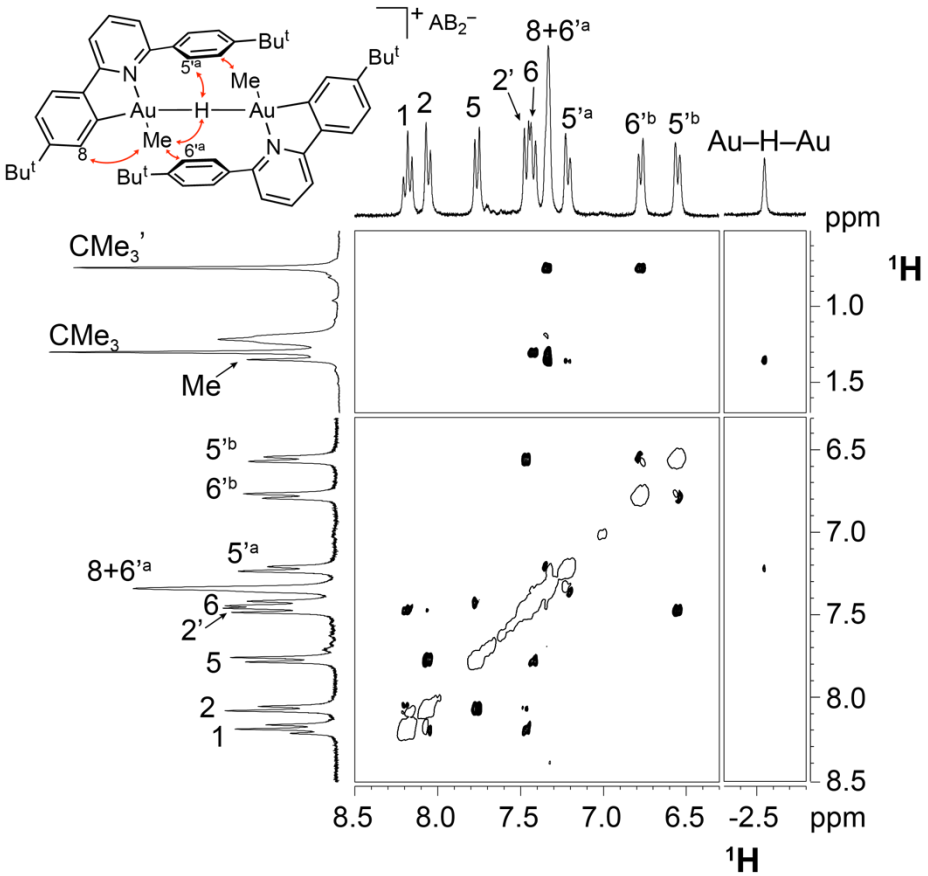

Figure S38. Four sections of the ^{1}H NOESY NMR spectrum of complex **22a** (253K, CD_2Cl_2).

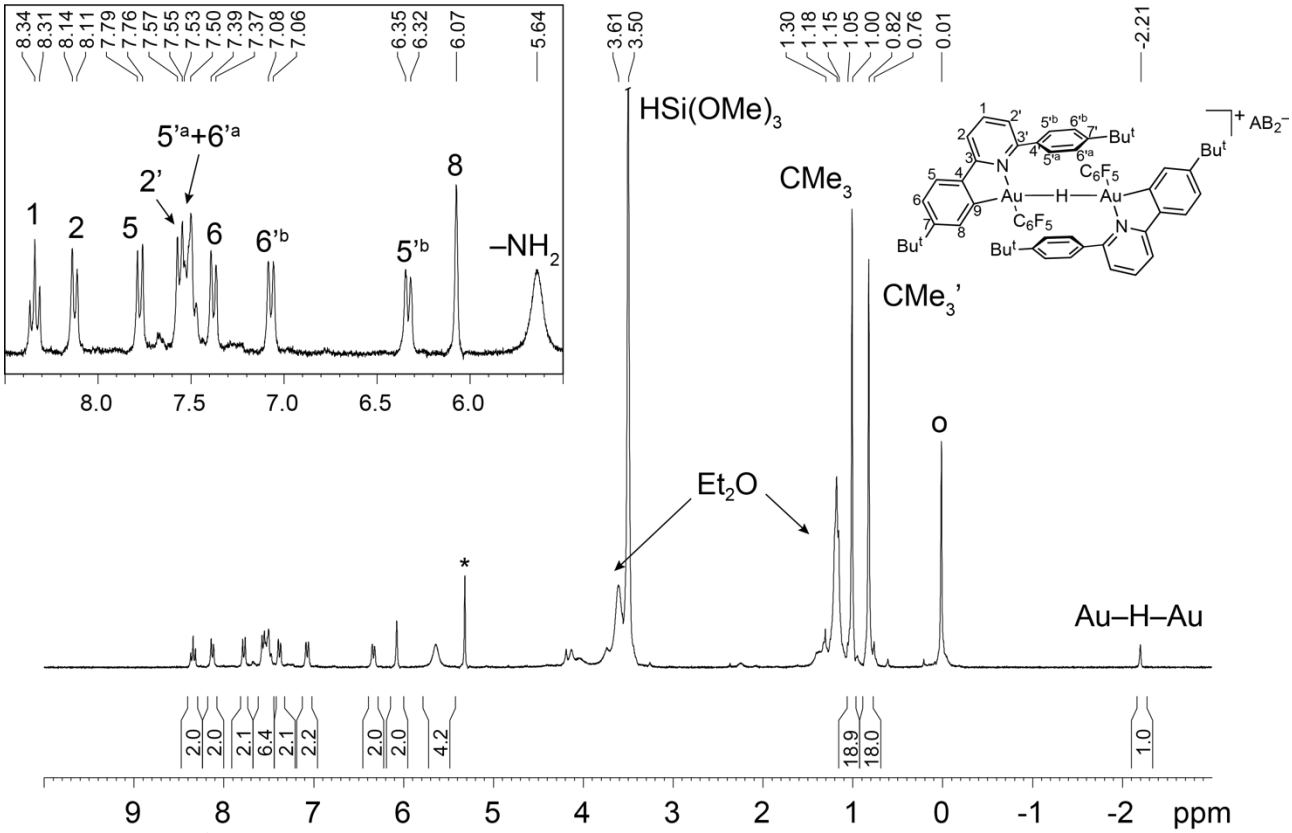

Figure S39. ^{1}H NMR spectrum of complex **22a** (253K, CD_2Cl_2); * denotes residual protonated CD_2Cl_2, o denotes silicone grease.

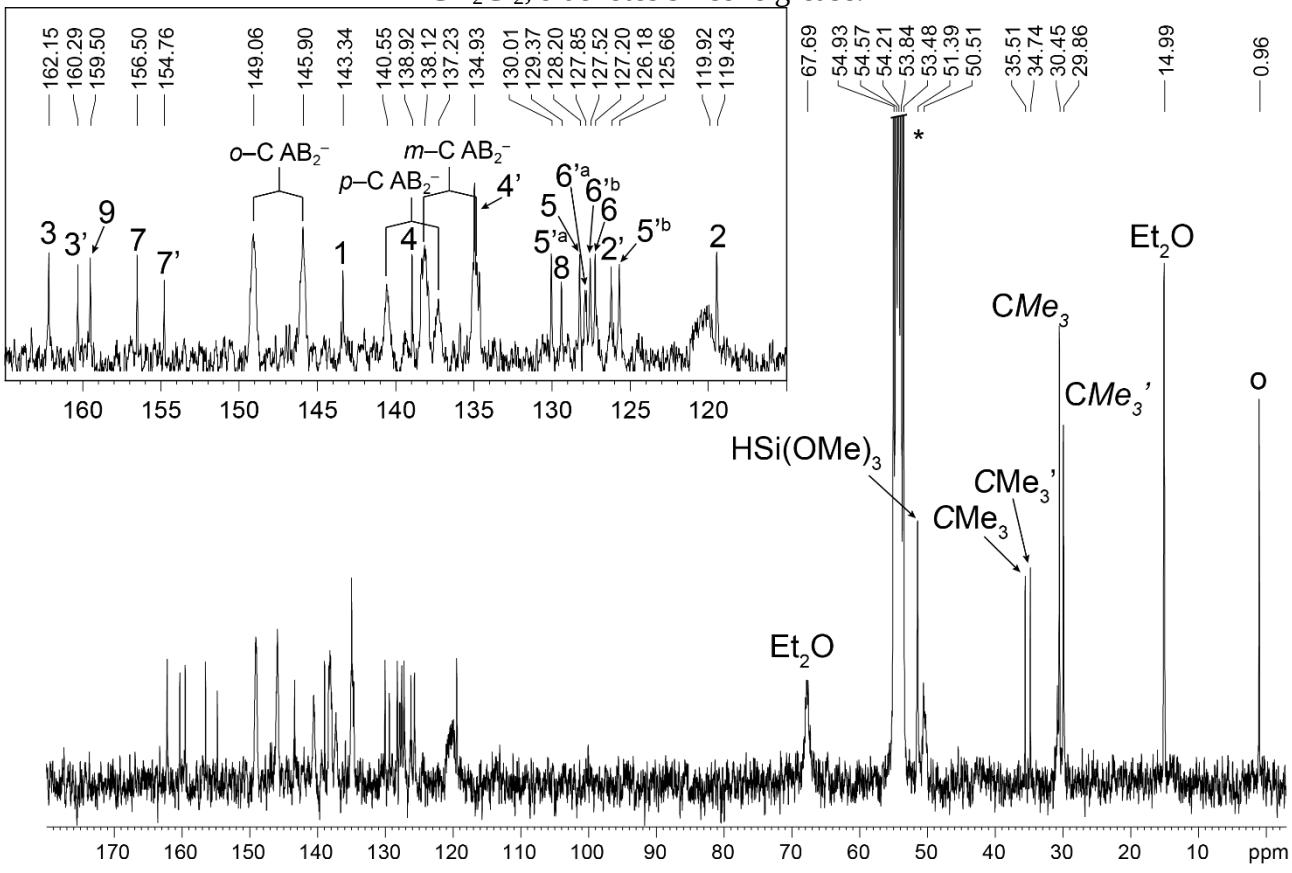

Figure S40. $^{13}C\{^{1}H\}$ NMR spectrum of complex **22b** (253K, CD_2Cl_2); * denotes CD_2Cl_2; AB_2^- $=H_2N[B(C_6F_5)_3]_2^-$.

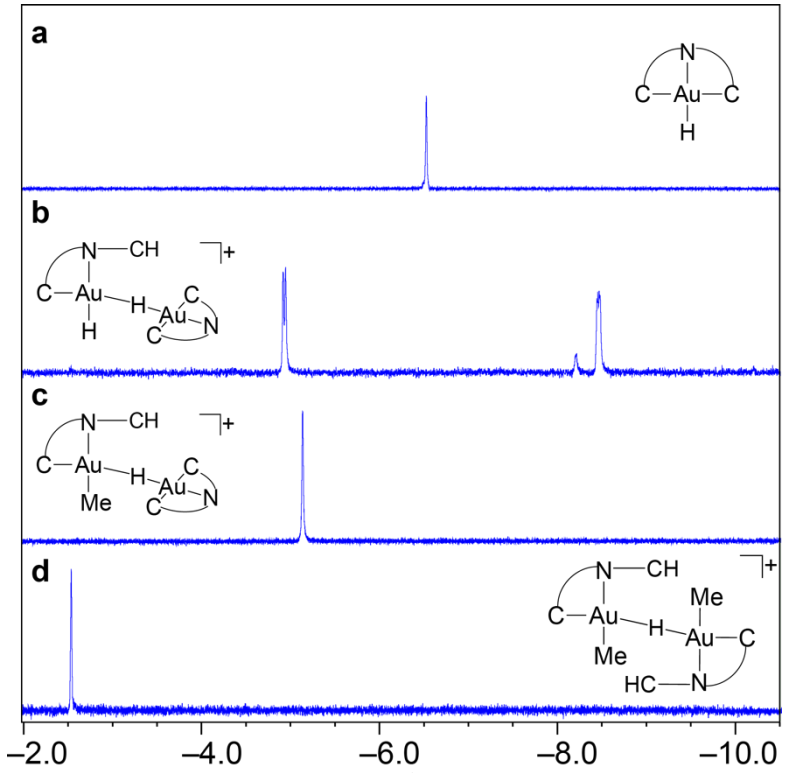

Figure S41. Overlay of the hydride regions of the ^{1}H NMR spectra of (a) (C^N^C)AuH, (b) **20**, (c) **21**, and (d) **22a** (in CD_2Cl_2, 213 K).

2. Photoisomerization Experiments

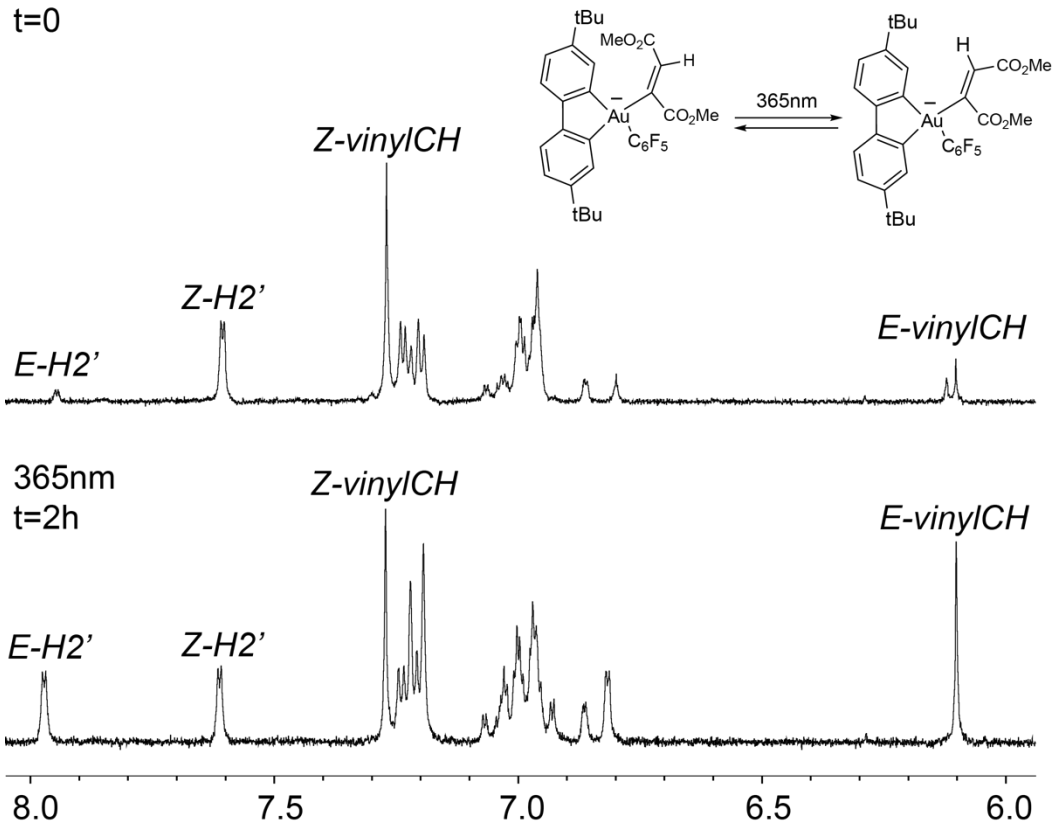

Figure S42. Evolution of the aromatic region of the ^{1}H NMR spectrum of **17** upon irradiation with UV light for 2 hours (room temperature, THF–d_8).

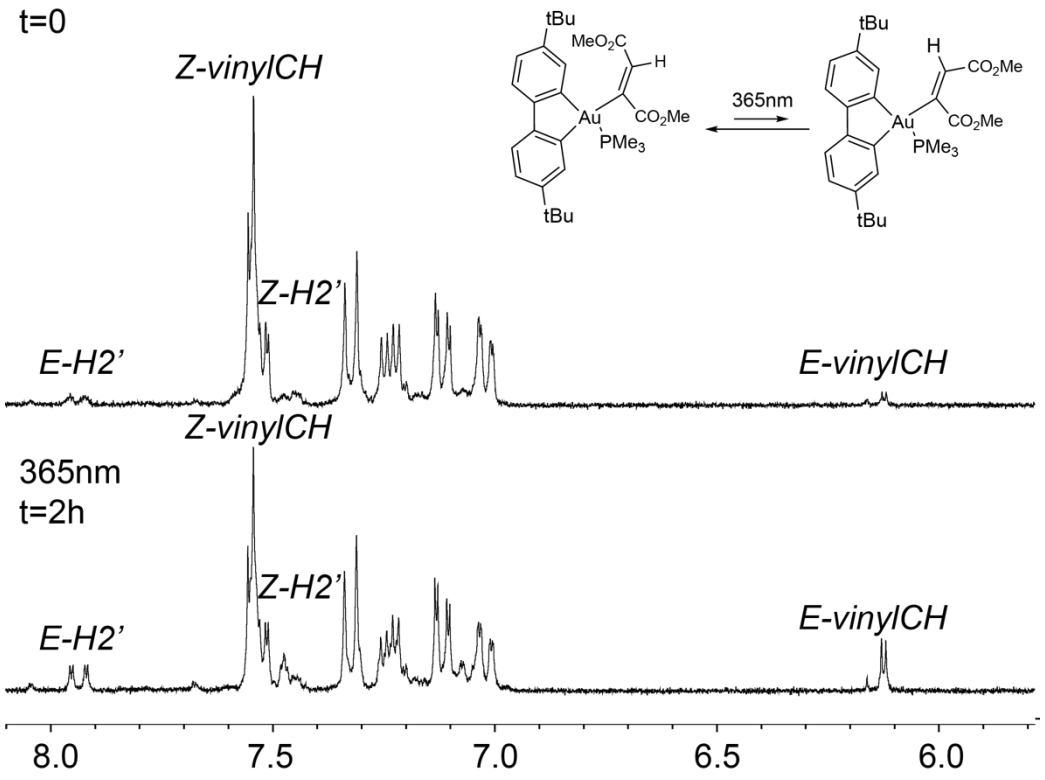

Figure S43. Evolution of the aromatic region of the ^{1}H NMR spectrum of **12** upon irradiation with UV light for 2 hours (room temperature, THF–d_8).

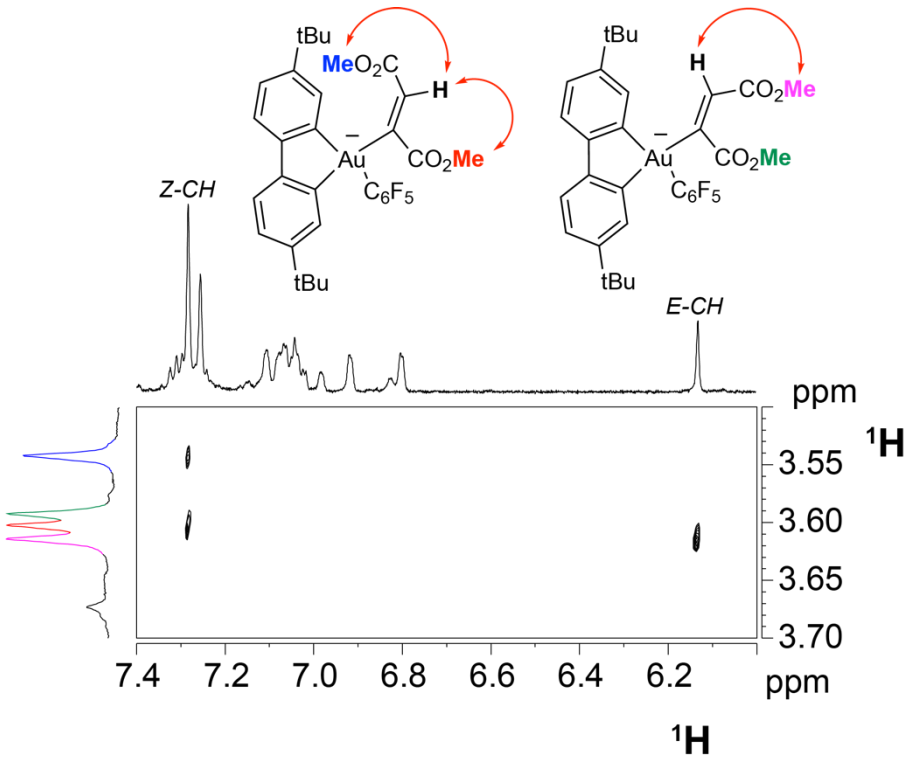

Figure S44. A section of the ^{1}H NOESY NMR spectrum of **17** after photoisomerization (297K, CD_2Cl_2).

3. X-Ray Crystallography

Complex **9**: colorless crystal grown by slow evaporation under N_2 of a solution of the crude in diethyl ether. The crystal was mounted on a MiTeGen MicroMesh and fixed in a cold nitrogen stream at 100 K. Diffraction intensities were recorded at 100 K on a Rigaku 007HF equipped with Varimax confocal mirrors and an AFC11 goniometer and Rigaku, HyPix 6000 detector with Enhance (Cu) X-ray Source. Data collection, refinement and reduction was performed using the CrysAlisPro 1.171.39.9g (Rigaku OD, 2015) suite of programs and the absorption correction performed at this stage.[S1] The structure was solved in $P2_1/n$ symmetry using SHELXT[S2] and refined by full-matrix least-squares methods on F^2 with SHELXL.[S3] The asymmetric unit is formed by four gold molecules and one molecule of diethyl ether, what arises to the stoichiometry **9**·1/4 Et_2O.

Non-hydrogen atoms were refined with anisotropic thermal parameters. The thermal parameters of some carbon atoms were modeled using EADP and ISOR restrictions to avoid alerts related with too large U_{eq} parameters compared with neighboring atoms. Hydrogen atoms, with the exception of the hydride atoms, were included in idealized positions. Several peaks of residual density were found in the final model but with no chemical meanings. No missed symmetry was reported by PLATON.[S4] Computer programs used in this analysis were run through WinGX.[S5] Scattering factors for neutral atoms were taken from reference [S6].

Complex **12**: Colorless plates grown by slow evaporation at room temperature of a saturated solution of the pure crude material in a mixture ca. 50:50 CH_2Cl_2:toluene. The crystal was mounted on a MiTeGen MicroMesh and fixed in a cold nitrogen stream at 100 K. Diffraction intensities were recorded at 100 K on a Rigaku FRE+ equipped with HF Varimax confocal mirrors and an AFC12 goniometer and HG Saturn 724+ detector with Mo K_α X-ray Source. Data collection, refinement and reduction was performed using the CrysAlisPro 1.171.39.9g (Rigaku OD, 2015) suite of programs and the absorption correction performed at this stage.[S1] The structure was solved using SHELXT[S2] and refined by full-matrix least-squares methods on F^2 with SHELXL.[S3] The crystal showed orthorhombic $P2_12_12_1$ symmetry with a Flack parameter of 0.421(3) indicative of a racemic crystal.[S7]

Non-hydrogen atoms were refined with anisotropic thermal parameters. Hydrogen atoms were included in idealized positions. No missed symmetry was reported by PLATON.[S4] Computer programs used in this analysis were run through WinGX.[S5] Scattering factors for neutral atoms were taken from reference [S6].

Complex **17**: Colorless crystals grown by slow diffusion of petrol into a saturated solution of the complex in CH_2Cl_2. The crystal was mounted on a MiTeGen MicroMesh and fixed in a cold

nitrogen stream at 100 K. Diffraction intensities were recorded at 100 K on a Rigaku FRE+ equipped with HF Varimax confocal mirrors and an AFC12 goniometer and HG Saturn 724+ detector with Mo K_α X-ray Source. Data collection, refinement and reduction was performed using the CrysAlisPro 1.171.39.9g (Rigaku OD, 2015) suite of programs and the absorption correction performed at this stage.[S1] The structure was solved in orthorhombic Pbca symmetry using SHELXT[S2] and refined by full-matrix least-squares methods on F^2 with SHELXL.[S3] No missed symmetry was reported by PLATON.[S4]

Non-hydrogen atoms were refined with anisotropic thermal parameters. Hydrogen atoms were included in idealized positions. The thermal parameters of some carbon atoms and O2 were modelled using EADP and ISOR restrictions to avoid alerts related with too large U_{eq} parameters compared with neighboring atoms. Several peaks of residual density were found in the final model but with no chemical meaning. The check-cif reveals two A alerts; the first one is generated by the residual electron density most likely due to a low quality of the crystal; the second A alert is generated by the presence of a short intermolecular H-H distance. However, this distance involves the NBu_4 groups and we observed positional disorder in the butyl groups that are most likely responsible of the problem. Our attempts to model this disorder gave poor convergence in the refinement. Computer programs used in this analysis were run through WinGX.[S5] Scattering factors for neutral atoms were taken from reference [S6].

[(C^C)(AuPMe$_3$)$_2$]$_x$ Orange crystals identified as [(C^C)(AuPMe$_3$)$_2$]$_x$ were found during the crystallization process of (C^C)AuH(PMe$_3$). One crystal was mounted on a MiTeGen MicroMesh and fixed in a cold nitrogen stream at 100 K. Diffraction intensities were recorded at 100 K on a Rigaku FRE+ equipped with HF Varimax confocal mirrors and an AFC12 goniometer and HG Saturn 724+ detector with Rigaku (Cu) X-ray Source. Data collection, refinement and reduction was performed using the CrysAlisPro 1.171.39.9g (Rigaku OD, 2015) suite of programs and the absorption correction performed at this stage.[S1] The structure was solved in monoclinic $P2_1/c$ symmetry using SHELXT[S2] and refined by full-matrix least-squares methods on F^2 with SHELXL.[S3] No missed symmetry was reported by PLATON.[S4] Non-hydrogen atoms were refined with anisotropic thermal parameters. Hydrogen atoms were included in idealized positions. The check-cif reveals the presence of one A alert related with a low fraction of measured theta but the model is unambiguous. Several peaks of residual density were found in the final model but with no chemical meaning. Computer programs used in this analysis were run through WinGX.[S5] Scattering factors for neutral atoms were taken from reference [S6].

[(C^C)Au(μ-OH)]$_2$: Yellow crystals of [(C^C)Au(μ-OH)]$_2$ were grown by slow evaporation in air of a diethyl ether solution of (C^C)AuH(Ptol$_3$). The crystal was mounted on a MiTeGen

MicroMesh and fixed in a cold nitrogen stream at 100 K. Diffraction intensities were recorded at 100 K on a Rigaku FRE+ equipped with HF Varimax confocal mirrors and an AFC12 goniometer and HG Saturn 724+ detector with Mo K_α X-ray Source. Data collection, refinement and reduction was performed using the CrysAlisPro 1.171.39.9g (Rigaku OD, 2015) suite of programs and the absorption correction performed at this stage.[S1] The structure was solved in monoclinic $P2_1/c$ symmetry using SHELXT[S2] and refined by full-matrix least-squares methods on F^2 with SHELXL.[S3] No missed symmetry was reported by PLATON.[S4] Non-hydrogen atoms were refined with anisotropic thermal parameters. Hydrogen atoms were included in idealized positions. Computer programs used in this analysis were run through WinGX.[S5] Scattering factors for neutral atoms were taken from reference [S6].

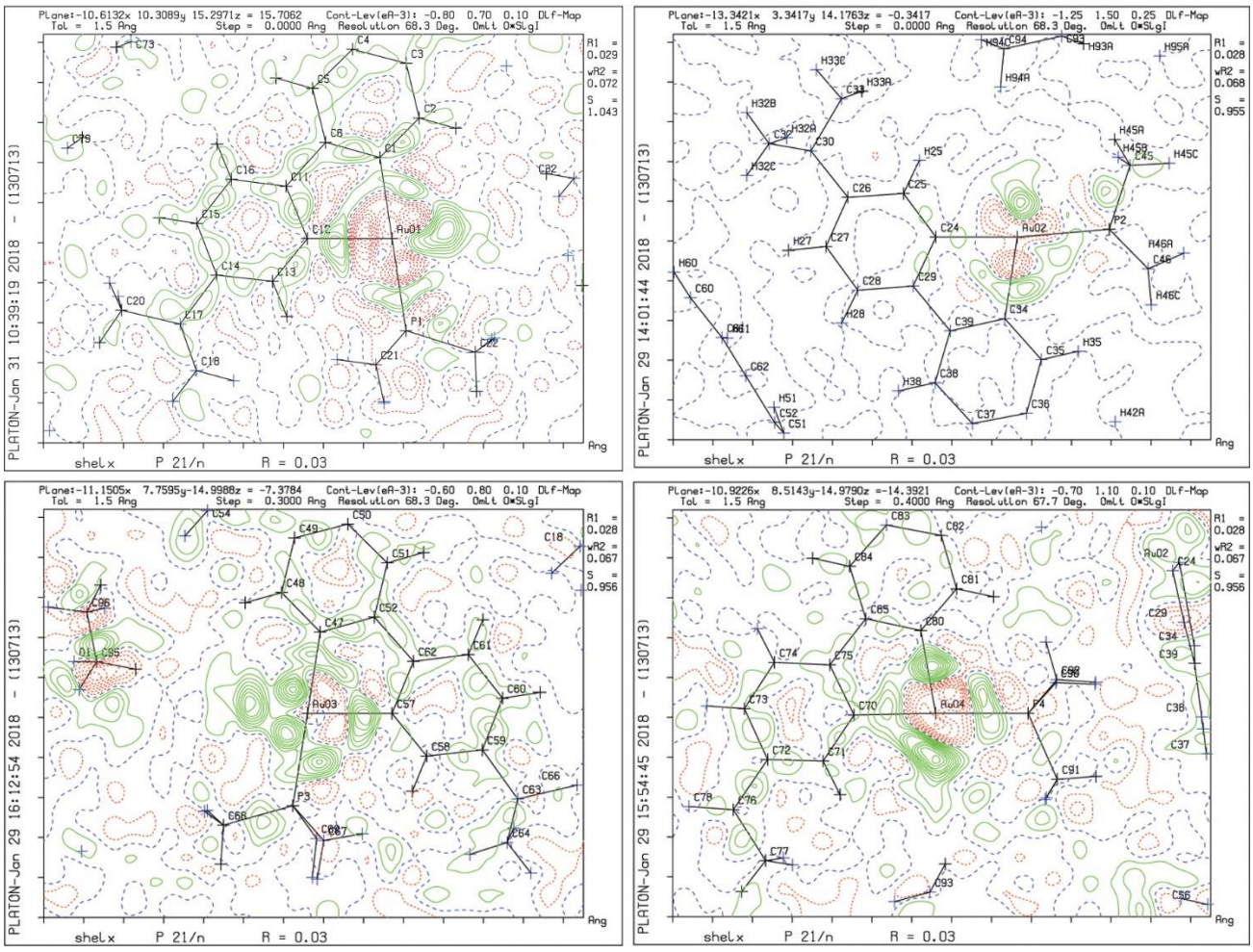

Figure S45. Electron density maps for each of the Au coordination planes of the 4 different molecules found in the asymmetric unit of complex **9** revealing the presence of negative regions indicative of the Au-H(hydride) bond.

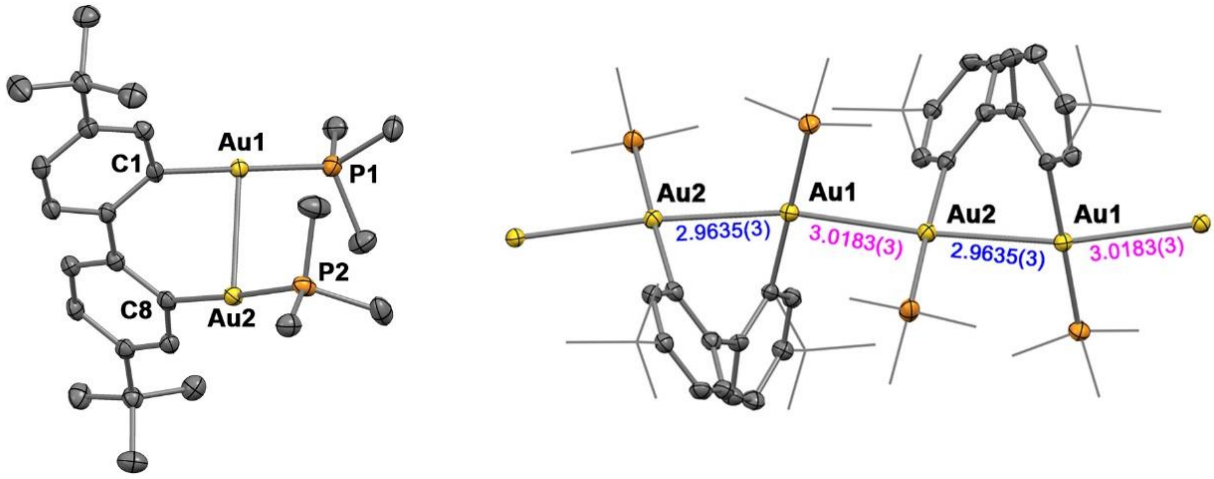

Figure S46. (left) Molecular view of[(C^C)(AuPMe$_3$)$_2$. Non-hydrogen atoms represented as ellipsoids with 50% probability level and hydrogens omitted for clarity. Selected bond distances (Å) and angles (º): Au1-C1 2.084(5), Au2-C8 2.076(4), Au1-P1 2.290(1), Au2-P2 2.293(1), Au1-Au2 2.9635(3), C1-Au1-P1 179.4(1), C8-Au2-P2 176.9(1), C1-Au1-Au2 76.3(1), C8-Au2-Au1 79.7(1), P1-Au1-Au2 103.22(3), P2-Au2-Au1 98.08(3), torsion C1-Au1-Au2-C8 71.1(2), P1-Au1-Au2-P2 73.00(5). (right) Part of the polymer chain of [(C^C)(AuPMe$_3$)$_2$]$_x$ showing aurophilic interactions.

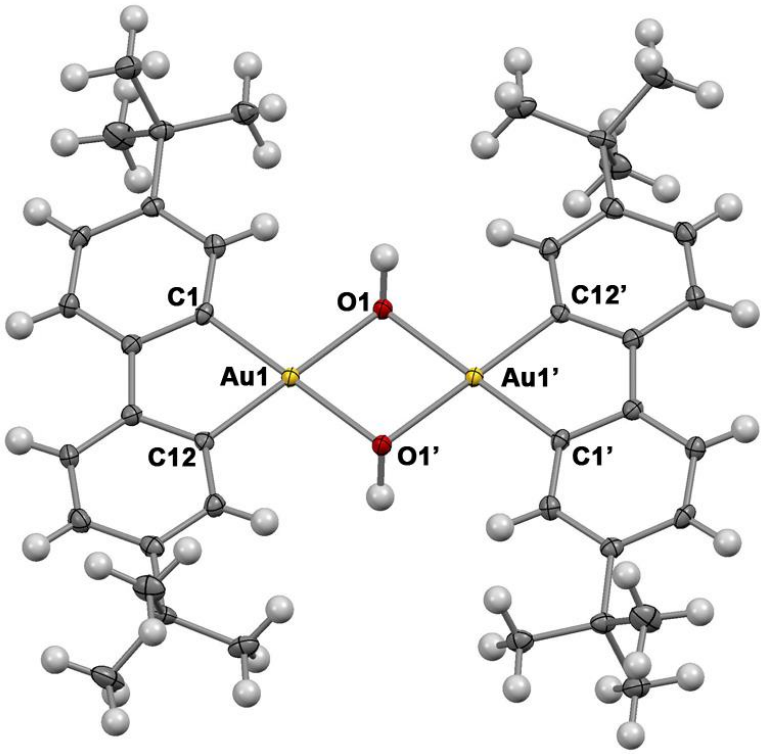

Figure S47. Molecular view of [(C^C)Au(μ-OH)]$_2$. Non-hydrogen atoms represented as ellipsoids with 50% probability level. Selected bond distances (Å) and angles (º): Au1-C1 2.002(3), Au1-C12 1.998(3), Au1-O1 2.113(2), Au1-O1' 2.118(2), C1-Au1-C12 81.1(1), C1-Au1-O1 99.5(1), O1-Au1-O1' 80.35(9), O1'-Au1-C12 99.1(1), C1-Au1-O1 178.4(1), C12-Au1-O1 178.8(1).

4. Computational Details

All structures were fully optimized at the PBE0 level of theory,[S8] including an atom-pairwise correction for dispersion forces via Grimme's D3 model[S9] with Becke–Johnson (BJ) damping[S10] in the Turbomole program package.[S11] A quasirelativistic energy-consistent small-core pseudopotential (effective-core potential, ECP)[S12,S13] in conjunction with Gaussian-type orbital valence basis sets of quality (8s7p6d1f)/[6s4p3d1f] and (11s10p8d2f)/[6s5p3d2f] was used for gold and iodine, respectively, whereas all other atoms have been treated with an all-electron def2-TZVP basis set.[S14] Frequency calculations at the same level of theory (PBE0-D3(BJ)/ECP/def2-TZVP) were performed to verify that all stationary points are minima with no imaginary frequency.

The two-component relativistic all-electron DFT calculations of the NMR nuclear shieldings[S15] and nuclear spin-spin *J*-couplings[S16] were performed using the Amsterdam Density Functional (ADF) program suite,[S17] employing the PBE0 exchange-correlation functional[S8] in conjunction with Slater-type orbital basis sets of triple-ζ doubly polarized (TZ2P) quality and an integration accuracy of 5.0. The ZORA calculations of NMR shieldings were done by using gauge-including atomic orbitals (GIAOs)[S18] and including the previously neglected terms from the exchange–correlation (XC) response kernel.[S19] The latter were shown to be particularly important for systems with large spin-orbit (SO) shielding contributions.[S20,S21] For comparative purposes, the nuclear shieldings were also evaluated using four-component, fully relativistic DFT calculations within the matrix Dirac-Kohn-Sham (mDKS) framework,[S22-S24] employing the PBE0 hybrid functional,[S8] as implemented in the ReSpect program package.[S25] The 4c-mDKS method combines GIAOs with restricted magnetically balanced (RMB) orbitals for the small component.[S22-S24] For heavy atoms (Z > 18), the Dyall VDZ[S26] basis set was used, along with fully uncontracted IGLO-II basis sets for light ligand atoms.[S27] An integration grid of "Adaptive" size for the Lebedev angular points was applied and the following numbers of radial grid points were used for the indicated atoms: H, B, C, N, O, F: 60; P, S, Cl: 72; I: 80; Au: 96. All 4c-mDKS calculations were performed without fitting the electron and spin densities. In the case of complexes with pendant alkyl chains, the bulky *tert*-butyl groups were replaced by hydrogen atoms in NMR shielding calculations (these were, however, kept in structure optimizations).

The computed ^{1}H nuclear shieldings were converted to chemical shifts (δ, in ppm) relative to the shielding of tetramethylsilane (TMS), considering (C^N^C)AuH (complex **A** in Chart 1) as a secondary standard, with a hydride shift value of –6.51 ppm (measured in CD_2Cl_2).[S28]

Molecular orbital (MO) analyses of the NMR shifts and natural localized molecular orbital (NLMO) analyses were carried out using the NBO 5.0 module[S29] in the ADF code. The (two identical) shielding contributions of degenerate MOs or spinors were summed and are reported as

contributions of one parental MO or spinor. When discussing the effect of a given occupied MO, the sum of the so-called U1 (first-order changes in MO coefficients) and S1 (first-order changes in overlap matrix) contributions reported by ADF are given, together with gauge contributions for the σ^{p} and σ^{p+SO} contributions.

Quantum theory of atoms-in-molecules (QTAIM)[S30] analyses were performed at the PBE0/def2-TZVP/ECP level, using the Multifwn[S31] program interfaced with Gaussian 09.[S32] In particular, we focused on QTAIM delocalization indices (DI), as a measure of the Au–H bond covalency. The DI integrates the electron density in the bonding region between two atoms in question and is closely related to the covalent bond order, reduced by bond polarity (i.e., DI = 1.0 for a "pure" covalent single bond, but DI = 0.0 for a "pure" ionic bond).

5. Results of Quantum-Chemical Calculations

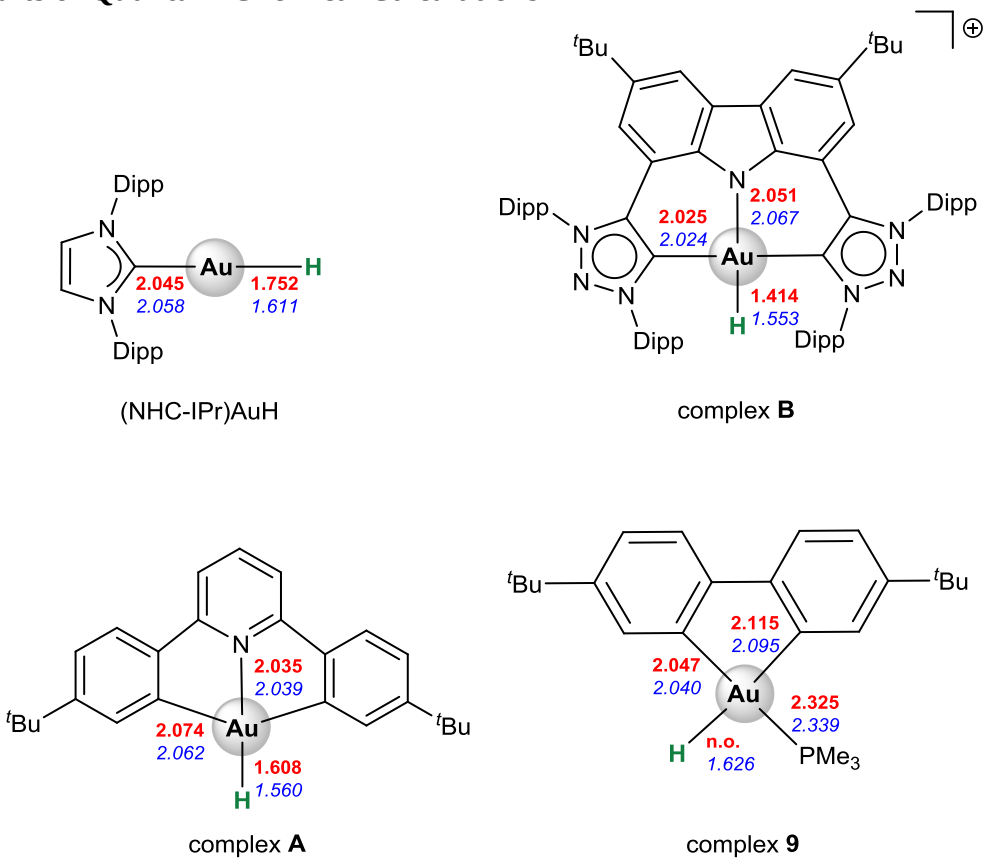

Figure S48. Comparison of selected Au–L bond distances (in Ångstroms) for X-ray (data in red) and DFT (PBE0-D3(BJ)/ECP/def2-TZVP) optimized (*data in blue*) structures of hitherto characterized gold hydride complexes. X-ray structural data for (NHC-IPr)AuH, (C^N^C)AuH (complex **A**) and (C^C^N)AuH (complex **B**) were taken from refs. [S33], [S28] and [S34], respectively. Complex **9** was characterized in this work.

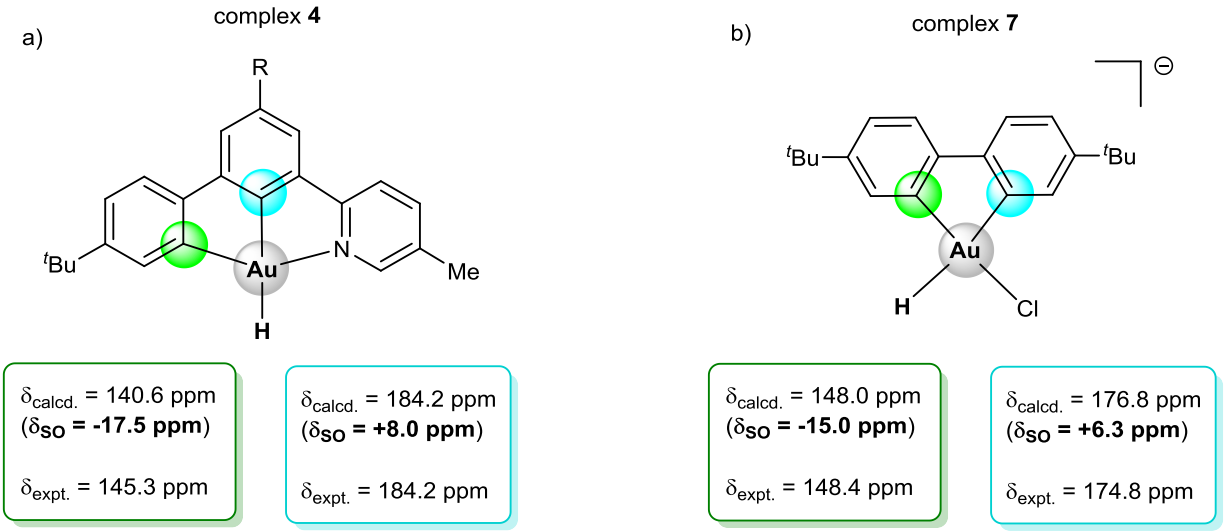

Figure S49. Computed and experimental ^{13}C NMR shifts (in ppm vs. TMS) for Au-bound carbon atoms in selected gold(III) hydride complexes. 2c-ZORA-SO/PBE0-XC/TZ2P results (cf. Computational details).

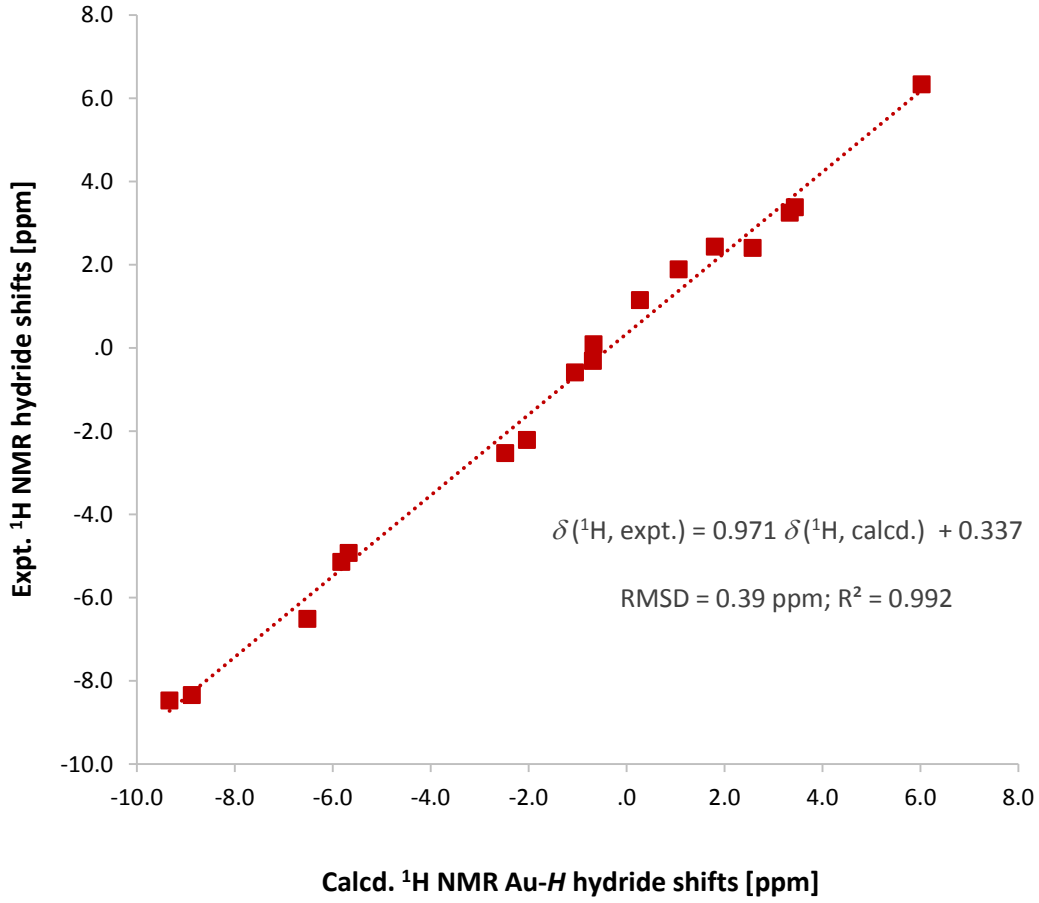

Figure S50. Comparison of experimental and calculated ^{1}H NMR hydride shifts (in ppm vs. TMS) for gold hydride complexes.

Table S1. DFT optimized Au–H bond-lengths (in Ångstroms), NPA atomic charges, NLMO composition of Au-H bonds and computed ^{1}H NMR hydride shieldings (in ppm) decomposed into diamagnetic (σ^{d}), paramagnetic (σ^{p}) and spin-orbit (σ^{SO}) contributions for a series of linear **HAu^{I}L^{q}** complexes [a]

	d(Au-H)	NPA charges		NLMO analysis of Au-H bonding			^{1}H NMR hydride shieldings (σ) and shifts (δ) (in ppm)				
L	[Å]	q(Au)	*q*(H)	%Au in Au-H	%Au(5d)	%Au.%Au(5d)	σ^{d}	σ^{p}	σ^{SO}	σ^{total}	δ(^{1}H)
OH_2	1.546	0.110	-0.184	42.7	19.3	8.2	31.2	3.2	10.2	44.6	-14.2
F^-	1.569	0.206	-0.374	34.5	21.2	7.3	33.0	3.5	7.6	44.1	-13.7
ONO_2^-	1.566	0.197	-0.330	39.4	19.4	7.6	32.4	2.4	6.6	41.4	-11.0
py	1.568	0.165	-0.258	39.9	19.1	7.6	31.8	1.6	5.1	38.5	-8.1
NH_3	1.566	0.120	-0.248	40.6	19.8	8.1	31.3	2.2	4.6	38.1	-7.7
NCS^-	1.581	0.222	-0.360	35.3	18.7	6.6	32.5	2.6	2.1	37.3	-6.9
Cl^-	1.587	0.147	-0.380	35.5	16.3	5.8	32.4	1.1	2.7	36.2	-5.8
SCN^-	1.599	0.127	-0.367	36.7	15.4	5.6	31.8	0.4	-0.4	31.8	-1.4
SH_2	1.584	0.102	-0.265	41.1	15.6	6.4	31.1	0.1	0.3	31.5	-1.1
I^-	1.598	0.098	-0.375	36.7	14.5	5.3	31.8	-0.4	-0.8	30.6	-0.2

	d(Au-H)	NPA charges		NLMO analysis of Au-H bonding			^{1}H NMR hydride shieldings (σ) and shifts (δ) (in ppm)				
L	[Å]	q(Au)	*q*(H)	%Au in Au-H	%Au(5d)	%Au.%Au(5d)	σ^{d}	σ^{p}	σ^{SO}	σ^{total}	$\delta(^{1}H)$
CN^-	1.623	0.164	-0.447	33.4	17.7	5.9	32.6	0.0	-4.9	27.7	2.7
$C_6H_5^-$	1.638	0.169	-0.466	32.9	18.0	5.9	32.0	0.0	-4.2	27.7	2.7
$C_6F_5^-$	1.621	0.178	-0.422	34.1	17.3	5.9	31.6	0.2	-4.2	27.6	2.8
CH_3^-	1.645	0.135	-0.486	32.6	17.6	5.7	31.8	0.2	-5.2	26.7	3.7
CO	1.607	0.257	-0.329	38.6	16.8	6.5	30.9	0.2	-7.0	24.1	6.3
H^-	1.660	0.016	-0.508	33.0	15.3	5.0	31.3	-0.6	-7.3	23.4	7.0
PH_3	1.612	0.141	-0.312	40.0	13.6	5.5	30.7	-1.3	-6.6	22.8	7.6
SiH_3^-	1.667	0.058	-0.487	34.2	12.1	4.1	30.8	-1.7	-11.1	18.0	12.4
Δ [b]	**0.121**		**0.324**				**2.3**	**5.2**	**21.3**		**26.6**

[a] Chemical shieldings computed at the 2c-ZORA(SO)/PBE0-XC/TZ2P level (cf. Computational details). [b] The difference between maximal and minimal value of the series.

Table S2. DFT optimized Au–H bond-lengths (in Ångstroms). NPA atomic charges. NLMO composition of Au-H bonds and computed ^{1}H NMR hydride shieldings (in ppm) decomposed into diamagnetic (σ^{d}), paramagnetic (σ^{p}) and spin-orbit (σ^{SO}) contributions for a series of ***trans*-[HAu^{III}(C_6H_5)$_2$L]^{q}** complexes [a]

	d(Au–H)	QTAIM	NPA charges		NLMO analysis of Au-H bonding			^{1}H NMR shieldings/shifts [ppm]			
L	[Å]	DI(Au–H)	q(Au)	*q*(H)	%Au	%Au(5d)	%Au.%Au(5d)	σ^{d}	σ^{p}	σ^{SO}	$\delta(^{1}H)$
OH_2	1.521	0.958	0.869	0.035	54.7	70.0	38.3	30.1	1.8	14.6	-16.1
ONO_2^-	1.530	0.956	0.936	-0.072	50.5	71.5	36.1	31.4	1.7	11.6	-14.3
F^-	1.534	0.957	0.975	-0.124	48.7	72.4	35.3	31.7	1.6	12.1	-14.0
NCS^-	1.540	0.957	0.944	-0.095	49.6	71.9	35.7	31.5	1.1	10.1	-12.2
py	1.539	0.945	0.890	-0.019	51.2	71.4	36.5	30.4	1.3	10.3	-11.6
NH_3	1.540	0.949	0.866	-0.024	53.2	69.8	37.1	29.9	1.4	10.0	-10.8
Cl^-	1.550	0.929	0.870	-0.113	51.0	70.1	35.7	31.0	-0.1	8.8	-9.2
SH_2	1.547	0.928	0.796	-0.015	52.2	68.1	35.5	29.9	-0.3	8.7	-7.8
I^-	1.563	0.920	0.808	-0.111	52.7	68.2	35.9	30.1	-1.0	8.6	-7.3
SCN^-	1.565	0.914	0.836	-0.116	51.9	69.4	36.0	30.5	-0.6	6.6	-6.1

	d(Au–H)	QTAIM	NPA charges		NLMO analysis of Au-H bonding			^{1}H NMR shieldings/shifts [ppm]			
L	[Å]	DI(Au–H)	q(Au)	*q*(H)	%Au	%Au(5d)	%Au.%Au(5d)	σ^d	σ^p	σ^{SO}	$\delta(^1H)$
CN^-	1.576	0.917	0.900	-0.202	48.0	70.3	33.7	32.0	-1.4	4.0	-4.1
CO	1.559	0.919	0.853	-0.062	53.1	69.4	36.8	30.0	-0.6	4.7	-3.7
$C_6F_5^-$	1.590	0.917	0.901	-0.195	48.2	69.7	33.6	30.1	0.0	3.2	-2.8
PH_3	1.571	0.908	0.786	-0.073	53.1	67.2	35.7	29.5	-1.2	3.5	-1.3
$C_6H_5^-$	1.613	0.894	0.916	-0.262	46.2	69.6	32.2	30.4	-0.4	1.5	-1.0
CH_3^-	1.625	0.890	0.901	-0.291	46.0	68.5	31.5	29.9	-0.4	-0.8	1.7
H^-	1.634	0.876	0.802	-0.343	46.2	67.4	31.1	30.6	-1.8	-1.5	3.2
SiH_3^-	1.646	0.873	0.765	-0.311	46.5	64.9	30.2	28.8	-1.1	-3.6	6.3
Δ [b]	**0.125**	**0.086**		**0.378**				**3.2**	**3.6**	**18.2**	**22.5**

[a] Chemical shieldings computed at the 2c-ZORA(SO)/PBE0-XC/TZ2P level (cf. Computational details). [b] The difference between maximal and minimal value of the series.

Table S3. DFT optimized Au–H bond-lengths (in Ångstroms). NPA atomic charges. NLMO composition of Au-H bonds and computed ^{1}H NMR hydride shieldings decomposed into diamagnetic (σ^{d}), paramagnetic (σ^{p}) and spin-orbit (σ^{SO}) contributions for a series of ***cis*-[HAu^{III}(bph)L]^{q}** complexes [a]

	d(Au–H)	QTAIM	NPA charges		NLMO analysis of Au-H bonding			^{1}H NMR shieldings/shifts [ppm]			
L	[Å]	DI(Au–H)	q(Au)	*q*(H)	%Au	%Au(5d)	%Au.%Au(5d)	σ^{d}	σ^{p}	σ^{SO}	$\delta(^{1}H)$
H^-	1.619	0.916	0.793	-0.314	44.3	68.4	30.3	30.3	0.3	0.5	-0.7
SCN^-	1.621	0.911	0.885	-0.296	44.4	70.7	31.4	31.7	-1.1	0.4	-0.6
CH_3^-	1.617	0.909	0.918	-0.302	44.6	69.2	30.9	30.5	-0.3	0.4	-0.2
SiH_3^-	1.618	0.910	0.760	-0.273	46.6	73.1	34.0	30.9	-0.5	-0.1	0.1
I^-	1.615	0.903	0.847	-0.286	45.5	69.5	31.6	30.7	-0.7	0.2	0.2
$C_6F_5^-$	1.619	0.901	0.942	-0.286	45.2	68.8	31.1	29.8	0.1	0.4	0.3
CN^-	1.619	0.900	0.927	-0.281	45.4	68.9	31.3	30.6	-0.6	0.0	0.4
NCS^-	1.622	0.896	1.016	-0.299	44.8	68.2	30.5	29.9	0.1	-0.1	0.6
$C_6H_5^-$	1.618	0.906	0.934	-0.288	45.0	68.9	31.0	30.2	-0.5	0.1	0.7
Cl^-	1.619	0.900	0.929	-0.304	44.6	68.0	30.3	30.8	-0.9	-0.3	0.8

	d(Au–H)	QTAIM	NPA charges		NLMO analysis of Au-H bonding			^{1}H NMR shieldings/shifts [ppm]			
L	[Å]	DI(Au–H)	q(Au)	*q*(H)	%Au	%Au(5d)	%Au.%Au(5d)	σ^d	σ^p	σ^{SO}	$\delta(^1H)$
ONO_2^-	1.624	0.897	1.012	-0.316	43.8	67.5	29.6	30.2	-0.4	-0.5	1.1
F^-	1.627	0.904	1.057	-0.337	42.9	65.9	28.3	30.3	-0.5	-0.5	1.1
PH_3	1.628	0.882	0.834	-0.285	45.4	70.0	31.8	30.2	-0.6	-1.2	2.1
SH_2	1.627	0.893	0.850	-0.307	44.9	67.7	30.4	30.5	-0.7	-1.5	2.2
NH_3	1.628	0.901	0.933	-0.324	43.8	66.4	29.1	29.8	-0.1	-2.0	2.7
py	1.626	0.896	0.955	-0.310	44.4	67.3	29.9	30.2	-1.0	-2.3	3.6
CO	1.627	0.881	0.927	-0.259	46.8	67.8	31.7	29.5	-0.4	-2.4	3.8
OH_2	1.633	0.874	0.937	-0.347	42.8	65.0	27.8	30.0	-0.4	-4.2	5.0
Δ [b]	**0.019**	**0.042**		**0.088**				**2.2**	**1.3**	**4.7**	**5.6**

[a] Chemical shieldings computed at the 2c-ZORA(SO)/PBE0-XC/TZ2P level (cf. Computational details). [b] The difference between maximal and minimal value of the series.

Table S4. DFT optimized Au–H bond-lengths (in Ångstroms). NPA atomic charges. NLMO composition of Au-H bonds and computed ^{1}H NMR hydride shieldings decomposed into diamagnetic (σ^{d}), paramagnetic (σ^{p}) and spin-orbit (σ^{SO}) contributions for a series of ***cis*-[HAu^{III}(ppy)L]$^{q+1}$** complexes [a]

	d(Au–H)	QTAIM	NPA charges		NLMO analysis of Au-H bonding			^{1}H NMR shieldings/shifts [ppm]			
L	[Å]	DI(Au–H)	q(Au)	*q*(H)	%Au	%Au(5d)	%Au.%Au(5d)	σ^{d}	σ^{p}	σ^{SO}	$\delta(^{1}H)$
ONO_2^-	1.547	0.955	1.013	-0.072	50.9	70.2	35.7	30.5	0.9	11.1	-12.0
NCS^-	1.545	0.952	1.021	-0.049	52.3	71.1	37.1	30.2	1.3	10.8	-11.9
F^-	1.547	0.957	1.054	-0.085	50.3	68.6	34.5	30.4	0.9	10.8	-11.7
SCN^-	1.543	0.960	0.863	-0.036	52.7	70.6	37.2	31.1	0.1	10.4	-11.1
Cl^-	1.543	0.942	0.916	-0.054	51.8	70.3	36.4	31.2	0.2	10.2	-11.1
I^-	1.543	0.941	0.916	-0.054	52.0	70.7	36.8	31.2	0.2	10.2	-11.1
H^-	1.544	0.953	0.782	-0.069	51.4	70.4	36.2	30.5	1.2	9.7	-10.9
CN^-	1.546	0.944	0.928	-0.043	52.1	70.2	36.6	30.8	0.5	9.8	-10.6
$C_6F_5^-$	1.544	0.958	0.935	-0.047	52.0	71.1	36.9	30.1	0.9	9.9	-10.4
CH_3^-	1.542	0.954	0.908	-0.065	51.3	70.4	36.1	30.6	0.7	9.0	-9.9

	d(Au–H)	QTAIM	NPA charges		NLMO analysis of Au-H bonding			^{1}H NMR shieldings/shifts [ppm]			
L	[Å]	DI(Au–H)	q(Au)	*q*(H)	%Au	%Au(5d)	%Au.%Au(5d)	σ^d	σ^p	σ^{SO}	$\delta(^1H)$
$C_6H_5^-$	1.545	0.953	0.923	-0.054	52.1	71.4	37.2	30.4	0.5	9.4	-9.9
SiH_3^-	1.548	0.950	0.748	-0.058	51.7	73.8	38.1	31.4	0.1	8.7	-9.7
NH_3	1.552	0.943	0.938	-0.078	50.9	69.9	35.5	30.0	1.0	8.9	-9.5
py	1.551	0.942	0.957	-0.062	51.6	70.3	36.3	30.2	0.3	9.3	-9.3
OH_2	1.556	0.946	0.936	-0.093	50.4	69.3	34.9	30.0	0.9	8.5	-9.0
PH_3	1.556	0.927	0.843	-0.062	51.4	72.1	37.1	30.6	0.2	8.1	-8.5
CO	1.560	0.918	0.918	-0.048	51.9	70.7	36.7	29.5	0.4	8.1	-7.6
SH_2	1.556	0.920	0.841	-0.064	52.2	69.2	36.1	30.3	0.5	6.8	-7.1
Δ [b]	**0.017**	**0.042**		**0.056**				**1.9**	**1.3**	**4.4**	**5.0**

[a] Chemical shieldings computed at the 2c-ZORA(SO)/PBE0-XC/TZ2P level (cf. Computational details). [b] The difference between maximal and minimal value of the series.

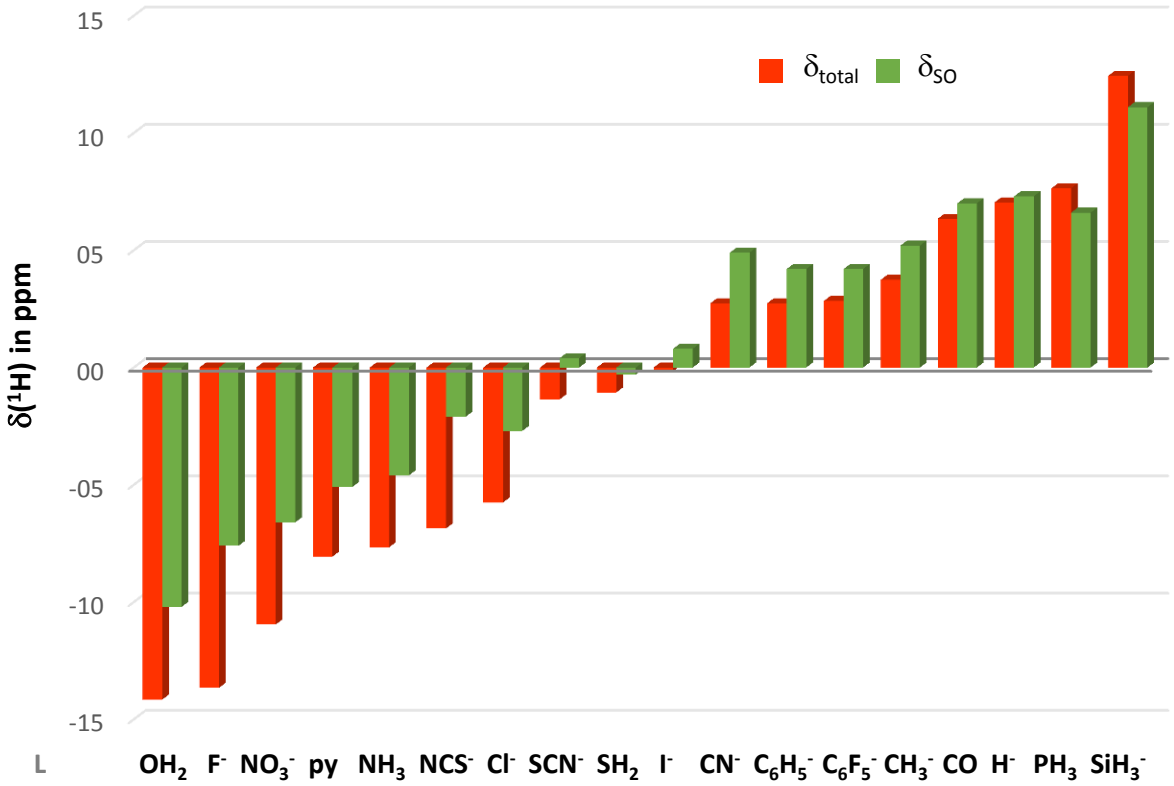

Figure S51. Dependence of the computed ^{1}H hydride shifts (δ_{total}) and spin-orbit-induced shift contributions (δ_{SO}) on the trans ligand L in the **HAuL^{q}** series (2c-ZORA(SO)/PBE0-XC/TZ2P results; cf. Table S1 for numerical data).

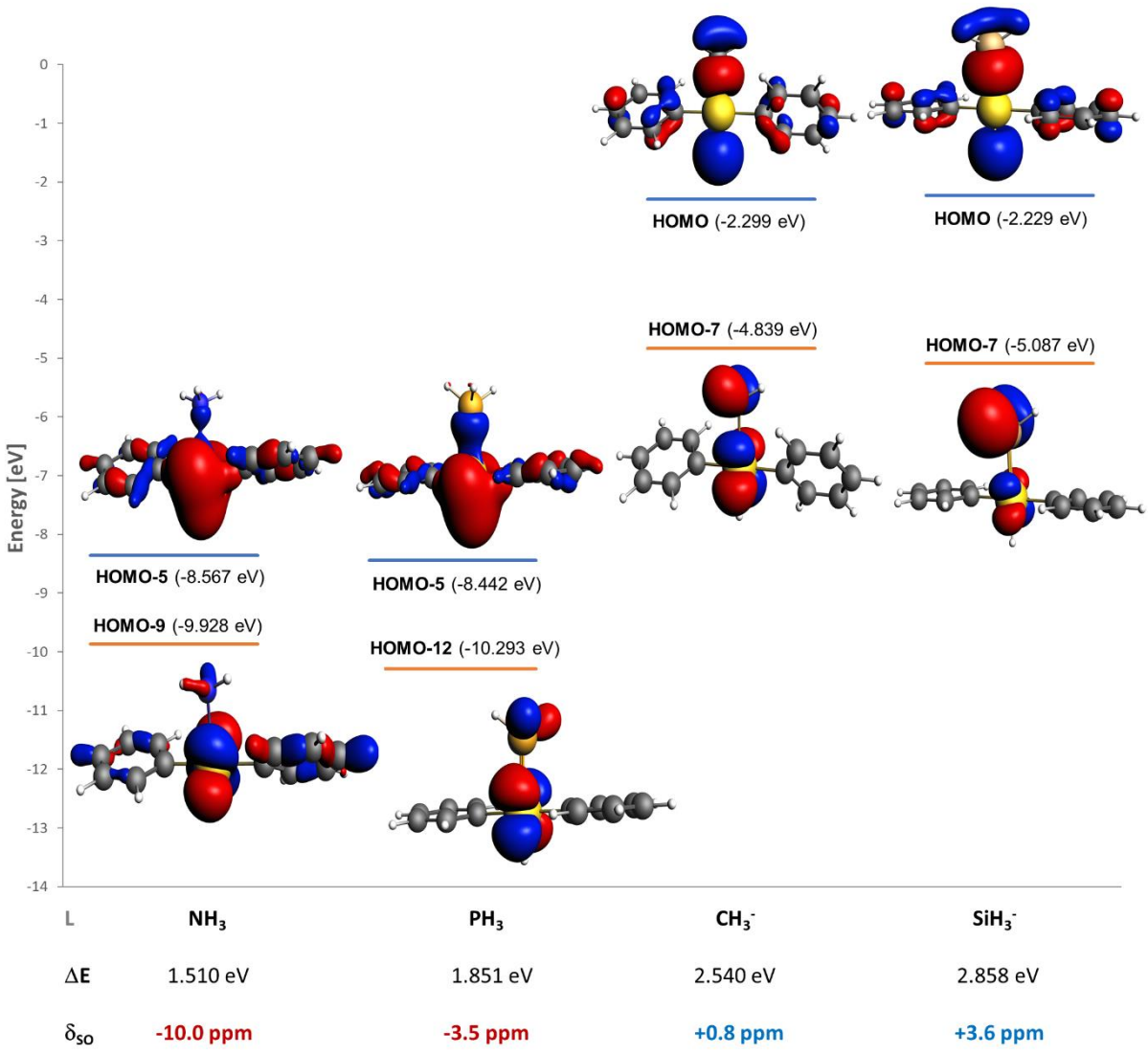

L	NH_3	PH_3	CH_3^-	SiH_3^-
ΔE	1.510 eV	1.851 eV	2.540 eV	2.858 eV
δ_{SO}	-10.0 ppm	-3.5 ppm	+0.8 ppm	+3.6 ppm

Figure S52. Energies of the highest occupied σ(Au-H)-type MOs (indicated by blue lines) and Au(d_π) orbitals (indicated by orange lines) in ***trans*-[HAu(C_6H_5)$_2$L]** series (L = NH_3, PH_3, CH_3^-, SiH_3^-). SR-ZORA/PBE0/TZ2P results.

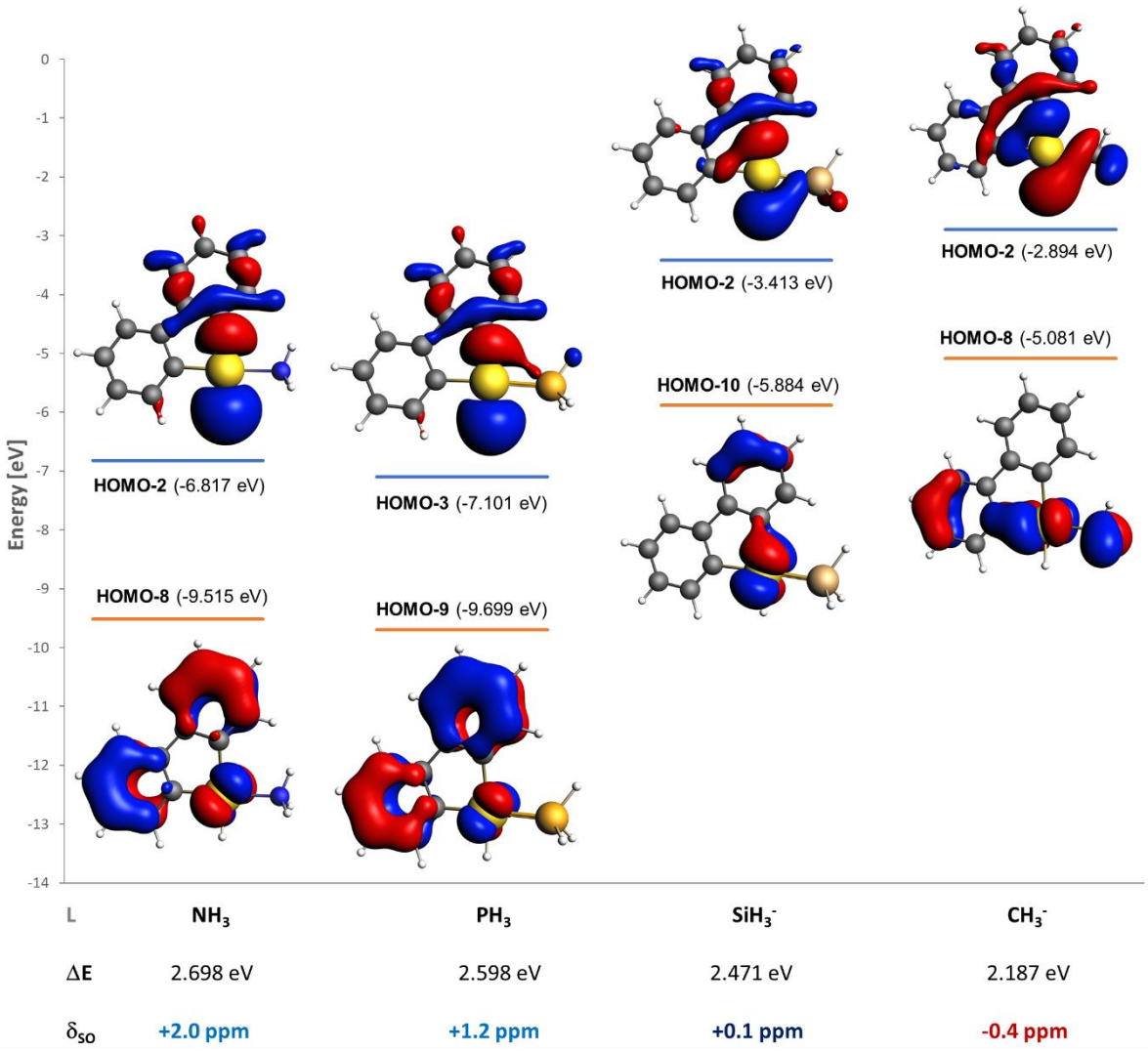

Figure S53. Energies of the highest occupied σ(Au-H)-type MOs (indicated by blue lines) and Au(d_π) orbitals (indicated by orange lines) in ***cis*-[HAu(bph)L]^q** series (L = NH_3, PH_3, CH_3^-, SiH_3^-). SR-ZORA/PBE0/TZ2P results.

6. References

[S1] a) Blessing, R. H. *Acta Cryst.* **1995**, *A51*, 33–38; b) Blessing, R. H., *Cryst. Rev.* **1987**, *1*, 3–58. (c) Blessing, R. H., *J. Appl. Cryst.* **1989**, *22*, 396–397.

[S2] Sheldrick, G. M. *Acta Cryst.* **2015**, *A71*, 3–8.

[S3] Sheldrick, G. M. *Acta Cryst.* **2008**, *A64*, 112–122.

[S4] a) Spek, A. L., PLATON–A Multipurpose Crystallographic Tool, Utrecht University, Utrecht, The Netherlands, **2006**; b) Spek, A. L. *Acta Cryst.* **1990**, *A46*, C34.

[S5] Farrugia, L. J. *J. Appl. Crystallogr*. **1999**, *32*, 837–838.

[S6] International Tables for X-ray Crystallography, Kluwer Academic Publishers, Dordrecht. Vol. C. **1992**, pp. 500, 219 and 193.

[S7] Flack, H. D. *Acta Crystallogr*. **1983**, *A39*, 876–881.

[S8] a) Perdew, J. P.; Burke, K.; Ernzerhof, M. *Phys. Rev. Lett.* **1996**, *77*, 3865–3868; b) Perdew, J. P.; Burke, K.; Ernzerhof, M. *Phys. Rev. Lett.* **1997**, *78*, 1396; c) Adamo, C.; Barone, V. *Chem. Phys. Lett.* **1998**. *298*. 113–119.

[S9] Grimme, S.; Antony, J.; Ehrlich, S.; Krieg. H. *J. Chem. Phys.* **2010**, *132*, 154104.

[S10] Grimme, S.; Ehrlich, S.; Goerigk, L. *J. Comp. Chem.* **2011**, *32*, 1456–1465.

[S11] Turbomole, version 7.0.2, A Development of University of Karlsruhe and Forschungszentrum Karlsruhe GmbH, 1989–2007; TURBOMOLE GmbH, since 2007; available from http://www.turbomole.com.

[S12] Andrae, D.; U. Häußermann, U.; Dolg, M.; Stoll, H.; Preuß, H. *Theor. Chim. Acta* **1990**, *77*, 123–141.

[S13] Dolg, M.; Wedig, U.; Stoll, H.; Preuß, H. *J. Chem. Phys.* **1987**, *86*, 866–872.

[S14] Weigend, F.; Ahlrichs, R. *Phys. Chem. Chem. Phys.* **2005**, *7*, 3297.

[S15] a) Schreckenbach, G.; Ziegler, T. *J. Phys. Chem.* **1995**, *99*, 606–611; b) Wolff, S. K.; Ziegler, T. *J. Chem. Phys.* **1998**, *109*, 895–905; c) Wolff, S. K.; Ziegler, T.; van Lenthe, E.; Baerends, E. J. *J. Chem. Phys.* **1999**, *110*, 7689–7698; d) Krykunov, M.; Ziegler, T.; van Lenthe, E. *Int. J. Quantum Chem.* **2009**, *109*, 1676–1683.

[S16] a) Autschbach, J.; Ziegler, T. *J. Chem. Phys.* **2000**, *113*, 936–947; b) Autschbach, J.; Ziegler, T. *J. Chem. Phys.* **2000**. *113*, 9410–9418; c) Autschbach, J. *J. Chem. Phys.* **2008**, *129*, 094105; d) Autschbach, J. *J. Chem. Phys.* **2009**, *130*, 209901.

[S17] Amsterdam Density Functional (ADF), version 2012.01, SCM, Theoretical Chemistry, Vrije Universiteit, Amsterdam, Netherlands, 2012; available from http://www.scm.com.

[S18] Hansen, A. E.; Bouman, T. D. *J. Chem. Phys.* **1985**, *82*, 5035–5047.

[S19] Autschbach, J. *Mol. Phys.* **2013**, *111*, 2544–2554.

[S20] Greif, A. H.; Hrobárik, P.; Hrobáriková, V.; Arbuznikov, A. V.; Autschbach, J.; Kaupp, M. *Inorg. Chem.* **2015**, *54*, 7199–7208.

[S21] Greif, A. H.; Hrobárik, P.; Autschbach, J.; Kaupp, M. *Phys. Chem. Chem. Phys.* **2016**, *18*, 30462–30474.

[S22] Komorovský, S.; Repiský, M.; Malkina, O. L.; Malkin, V. G.; Ondík, I. M.; Kaupp, M. *J. Chem. Phys.* **2008**, *128*, 104101.

[S23] Komorovský, S.; Repiský, M.; Malkina, O. L.; Malkin, V. G. *J. Chem. Phys.* **2010**, *132*, 154101.

[S24] Hrobárik, P.; Hrobáriková, V.; Meier, F.; Repiský, M.; Komorovský, S.; Kaupp, M. *J. Phys. Chem. A* **2011**, *115*, 5654−5659.

[S25] ReSpect, version 4.0, 2017; Relativistic Spectroscopy Program; Repiský, M.; Komorovský, S.; Malkin, V. G.; Malkina, O. L.; Kaupp, M.; Ruud, K. with contributions from Bast, R.; Ekstrom, U.; Knecht, S.; Konečný, L.; Malkin-Ondík, I.; Malkin, E.; available from www.respectprogram.org.

[S26] Dyall, K. G. *Theor. Chem. Acc.* **2004**, *112*, 403–409

[S27] Kutzelnigg, W.; Fleischer, U.; Schindler, M. The IGLO-Method: Ab-initio Calculation and Interpretation of NMR Chemical Shifts and Magnetic Susceptibilities. In NMR Basic Principles and Progress. Diehl, P.; Fluck, E.; Günther, H.; Kosfeld, R.; Seelig, J.. Eds. Springer-Verlag: Berlin, 1991; Vol. 213, pp 165−262.

[S28] Roşca, D. A.; Smith, D. A.; Hughes, D. L.; Bochmann, M. *Angew. Chem. Int. Ed.* **2012**, *51*, 10643−10646.

[S29] Glendening, E. D.; Badenhoop, J. K.; Reed, A. E.; Carpenter, J. E.; Bohmann, J. A.; Morales, C. M.; Weinhold, F. NBO 5.0; Theoretical Chemistry Institute, University of Wisconsin: Madison, WI, 2001; available from http://nbo.chem.wisc.edu.

[S30] a) Bader, R. W. B. Atoms in Molecules: A Quantum Theory; Oxford University Press: Oxford, U.K., 1990. (b) Matta, C. F.; Boyd, R. J. The Quantum Theory of Atoms in Molecules; Wiley-VCH: Weinheim, Germany, 2007.

[S31] a) Lu, T. Multiwfn: A Multifunctional Wave Function Analyzer, version 3.3.7, 2015, available from http://sobereva.com/multiwfn; b) Lu, T.; Chen, F. W. *J. Comput. Chem.* **2012**, *33*, 580.

[S32] Gaussian 09, revision D.01, M. J. Frisch, G. W. Trucks, H. B. Schlegel, G. E. Scuseria, M. A. Robb, J. R. Cheeseman, G. Scalmani, V. Barone, B. Mennucci, G. A. Petersson, H. Nakatsuji, M. Caricato, X. Li, H. P. Hratchian, A. F. Izmaylov, J. Bloino, G. Zheng, J. L. Sonnenberg, M. Hada, M. Ehara, K. Toyota, R. Fukuda, J. Hasegawa, M. Ishida, T.

Nakajima, Y. Honda, O. Kitao, H. Nakai, T. Vreven, J. A. Montgomery, Jr., J. E. Peralta, F. Ogliaro, M. Bearpark, J. J. Heyd, E. Brothers, K. N. Kudin, V. N. Staroverov, R. Kobayashi, J. Normand, K. Raghavachari, A. Rendell, J. C. Burant, S. S. Iyengar, J. Tomasi, M. Cossi, N. Rega, J. M. Millam, M. Klene, J. E. Knox, J. B. Cross, V. Bakken, C. Adamo, J. Jaramillo, R. Gomperts, R. E. Stratmann, O. Yazyev, A. J. Austin, R. Cammi, C. Pomelli, J. W. Ochterski, R. L. Martin, K. Morokuma, V. G. Zakrzewski, G. A. Voth, P. Salvador, J. J. Dannenberg, S. Dapprich, A. D. Daniels, Ö. Farkas, J. B. Foresman, J. V. Ortiz, J. Cioslowski, and D. J. Fox, Gaussian, Inc., Wallingford CT, **2009**.

[S33] Tsui, E. Y.; Müller, P.; Sadighi, J. P. *Angew. Chem. Int. Ed.* **2008**, *47*, 8937–8940.

[S34] Kleinhans, G.; Hansmann, M. M.; Guisado-Barrios, G.; Liles, D. C.; Bertrand, G.; Bezuidenhout, D. I. *J. Am. Chem. Soc.* **2016**, *138*, 15873−15876.